WISDOM Project - XV. The link between circumnuclear molecular gas reservoirs and active galactic nucleus fuelling

Jacob S. Elford,[1]⋆ Timothy A. Davis,[1] Ilaria Ruffa,[1] Martin Bureau,[2] Michele Cappellari,[2] Jindra Gensior,[3] Satoru Iguchi,[4,5] Fu-Heng Liang,[2] Lijie Liu,[6,7] Anan Lu,[8] Thomas G. Williams[2,9]

[1]*Cardiff Hub for Astrophysics Research & Technology, School of Physics & Astronomy, Cardiff University, Queens Buildings, The Parade, Cardiff, CF24 3AA, UK*
[2]*Sub-department of Astrophysics, Department of Physics, University of Oxford, Denys Wilkinson Building, Keble Road, Oxford OX1 3RH, UK*
[3]*Institute for Computational Science, University of Zürich, Winterthurerstrasse 190,8057 Zürich*
[4]*Department of Astronomical Science, SOKENDAI (The Graduate University of Advanced Studies), Mitaka, Tokyo 181-8588, Japan*
[5]*National Astronomical Observatory of Japan, National Institutes of Natural Sciences, Mitaka, Tokyo 181-8588, Japan*
[6]*Cosmic Dawn Center (DAWN)*
[7]*DTU-Space, Technical University of Denmark, Elektrovej 327, DK-2800 Kgs, Lyngby , Denmark*
[8]*McGill Space Institute and Department of Physics, McGill University, 3600 rue University, Montreal, QC H3A 2T8, Canada*
[9]*Max Planck Institut für Astronomie, Königstuhl 17, 69117 Heidelberg, Germany*

ABSTRACT

We use high-resolution data from the millimetre-Wave Interferometric Survey of Dark Object Masses (WISDOM) project to investigate the connection between circumnuclear gas reservoirs and nuclear activity in a sample of nearby galaxies. Our sample spans a wide range of nuclear activity types including radio galaxies, Seyfert galaxies, low-luminosity active galactic nuclei (AGN) and inactive galaxies. We use measurements of nuclear millimetre continuum emission along with other archival tracers of AGN accretion/activity to investigate previous claims that at, circumnuclear scales ($<100\,\mathrm{pc}$), these should correlate with the mass of the cold molecular gas. We find that the molecular gas mass does not correlate with any tracer of nuclear activity. This suggests the level of nuclear activity cannot solely be regulated by the amount of cold gas around the supermassive black hole (SMBH). This indicates that AGN fuelling, that drives gas from the large scale galaxy to the nuclear regions, is not a ubiquitous process and may vary between AGN type, with timescale variations likely to be very important. By studying the structure of the central molecular gas reservoirs, we find our galaxies have a range of nuclear molecular gas concentrations. This could indicate that some of our galaxies may have had their circumnuclear regions impacted by AGN feedback, even though they currently have low nuclear activity. On the other hand, the nuclear molecular gas concentrations in our galaxies could instead be set by secular processes.

Key words: galaxies: ISM - galaxies: active - galaxies: nuclei

1 INTRODUCTION

It has been established that a supermassive black hole (SMBH) exists at the centre of **almost all** massive galaxies ($M_* \gtrsim 10^9\,\mathrm{M_\odot}$). A large number of studies have shown that tight correlations exist between the masses of such SMBHs and the properties of their host galaxies (such as the bulge mass: e.g. Magorrian et al. 1998; Marconi & Hunt 2003 and velocity dispersion: e.g. Ferrarese & Merritt 2000; Tremaine et al. 2002; Gültekin et al. 2009), suggesting a self-regulated co-evolution between them (see e.g. Kormendy & Ho 2013 for a review). There is evidence that active galactic nuclei (AGN) and the associated energetic output can play a crucial role in setting up and maintaining SMBH-host galaxy co-evolution, as it can change the physical conditions of the surrounding interstellar medium (ISM) and/or expel it from the nuclear regions (e.g. Bower et al. 2006; Croton et al. 2006; King & Pounds 2015; Morganti 2017;

Harrison 2017). The many details of these processes, however, are still poorly understood.

In the local Universe ($z < 0.1$), the AGN population can be separated into two main (non-exclusive) groups, differentiated by the mode of dominant energetic output: radiative and kinetic (e.g. Heckman & Best 2014). In the former the accretion occurs at high rates ($\gtrsim 1\%$ of the Eddington limit) through optically-thick and geometrically-thin discs (Shakura & Sunyaev 1973). This mode is radiatively efficient, so the dominant energy output is from the conversion of the potential energy of the matter accreted onto each SMBH into electromagnetic radiation. Kinetic-mode AGN instead produce little radiation and channel the bulk of the energy generated from the accretion process into collimated outflows of non-thermal plasma (i.e. radio jets). In these objects the geometrically-thin accretion disc is absent or truncated at some inner radii and likely replaced by geometrically-thick, optically-thin advection-dominated accretion flows (i.e. ADAFs; Narayan & Yi 1995), whereby the mate-

⋆ E-mail: elfordj@cardiff.ac.uk

rial is accreted onto the SMBH at low rates ($\ll 1\%$ of the Eddington limit).

Nearby radiative-mode AGN with weak or no radio jet emission have historically been called Seyfert galaxies. These objects possess all the characteristics of the "conventional" AGN described in the framework of the standard unified model (e.g. Antonucci 1993; Urry & Padovani 1995), and are typically hosted by late Hubble type galaxies (e.g. Martini et al. 2003). AGN producing strong kinetic feedback are instead called radio galaxies (RGs) and - based on their optical spectra - can be divided into two main classes (e.g. Best & Heckman 2012): high-excitation radio galaxies (HERGs) and low-excitation radio galaxies (LERGs). The former show strong high-ionisation (Seyfert-like) emission lines in their optical spectra, produce both radiative and kinetic AGN feedback, and are typically hosted by massive ($M_\star \gtrsim 10^{9.5}\,M_\odot$) early-type galaxies (ETGs). LERGs show no or weak, LINER (low-ionisation nuclear emission-line region)-like emission lines in their optical spectra, produce almost exclusively kinetic feedback, and are typically found in **very massive ($M_\star \gtrsim 10^{11}\,M_\odot$) ETGs**. Understanding the source of SMBH fuelling in the AGN populations introduced above is crucial to putting constraints on the physical processes driving and regulating the SMBH-host galaxy co-evolution. Up to now, however, a general picture for the fuelling of active SMBHs in the local Universe is still missing.

The central regions of Seyfert galaxies have been often observed to be dominated by cold atomic and molecular gas (e.g. Combes et al. 2013; García-Burillo et al. 2014), suggesting a potential connection with their nuclear activities. The finding by Izumi et al. (2016) of a positive correlation between the mass of ≈ 100pc-scale circumnuclear disks (CNDs) of dense molecular gas and the black hole mass accretion rate in nearby Seyferts seems to support this hypothesis. More recently, García-Burillo et al. (2021) also found that nuclear activity in these objects can cause deficits in their circumnuclear molecular gas reservoirs, with a negative trend between nuclear 2-10 keV X-ray luminosity and the central gas concentration. In both cases, however, the studies have been conducted on small samples of about 10 objects spanning relatively small ranges of Eddington ratios[1] ($\lambda_{\rm Edd} \sim 10^{-5} - 10^{-0.3}$), AGN luminosities ($L_{2-10\rm keV} \sim 10^{41} - 10^{44}$ **erg s**$^{-1}$) and host galaxy properties (almost exclusively barred spirals). It is therefore currently not clear whether or not the inferred cold gas-nuclear activity connection would hold over **a broader population of active galaxies**.

On the other hand, a long-established scenario suggests that the HERG/LERG dichotomy may be a consequence of different sources for the accreting gas. In this framework, HERGs are fuelled at relatively high rates by cold gas acquired from merging or collisions with gas-rich galaxies (e.g. Best & Heckman 2012). LERGs are instead powered by the accretion of hot gas from the intergalactic medium (IGM) through Bondi spherical accretion (Bondi 1952; Hardcastle et al. 2007). This hypothesis was initially supported by studies finding a correlation between jet power and Bondi accretion rate in LERGs (e.g Allen et al. 2006; Hardcastle et al. 2007; Balmaverde et al. 2008). Over the past decade, however, strong evidence has been acquired that cold gas can also play a role in fuelling LERGs, as large masses of cold gas and dust have been often observed at the centres of these objects (i.e. $M_{\rm H_2} \sim 10^7 - 10^{10}$ $M_\odot$; Prandoni et al. 2010; Ocaña Flaquer et al. 2010; North et al. 2019; Ruffa et al. 2019a,b, 2022).

The *total* molecular gas mass of a sample of nearby ETGs (most of which are LERG hosts) have also been observed to correlate with the AGN jet power, providing further evidence of a close connection between the two (Babyk et al. 2019). Models for cold gas SMBH fuelling in typical LERG hosts have been also developed and imply that the observed cold gas reservoirs originate from cooling of the hot X-ray emitting surrounding halos, either directly and smoothly (e.g. Negri et al. 2014) or after chaotic cooling (as predicted in chaotic cold accretion models, CCA; e.g. King & Pringle 2007; Wada et al. 2009; Nayakshin et al. 2012; Gaspari et al. 2013, 2015, 2017; King & Nixon 2015). Growing observational evidence provide support to this picture, at least for LERGs located in high-density environments (i.e. in rich groups and clusters). The importance of (chaotic) hot gas cooling in more isolated LERGs is still not clear (e.g. Ruffa et al. 2022).

In general, both theoretical studies (e.g. Shlosman et al. 1989) and numerical simulations (e.g. Pizzolato & Soker 2005, 2010; Wagner et al. 2012; McNamara et al. 2016) have shown that cold gas can play a fundamental role in fuelling nearby AGN (in both radiative and kinetic mode), with Ward et al. (2022) finding that AGN are preferentially located in galaxies with high molecular gas fractions. **A corresponding comprehensive observational picture, however, is still missing.**

The mm-Wave Interferometric Survey of Dark Object Masses (WISDOM) project is exploiting high-resolution CO observations from the Atacama Large Millimeter/submillimeter Array (ALMA) with the primary aim of measuring SMBH masses in a morphologically-diverse sample of nearby galaxies (e.g. Onishi et al. 2017; Davis et al. 2017, 2018; Smith et al. 2019; North et al. 2019; Smith et al. 2021a,b; North et al. 2021; Lelli et al. 2022; Ruffa et al. 2023). In this paper, we use WISDOM data with a typical spatial resolution of ~20–30 pc to look for a connection between the *circumnuclear* molecular gas reservoirs observed with ALMA and the SMBH fuelling across a sample with **wide** a range of nuclear activities (from low/high luminosity Seyferts to LERGs). Our main aim is to explore the scenarios described above, testing the cold gas-SMBH fuelling correlations and the scales over which it persists.

This paper is organised as follows. In Section 2, we describe the sample and the multi-wavelength observations used for our analysis. We describe the adopted methodology in 3. We present our results in Section 4 and discuss them in Section 5, before summarising and concluding in Section 6.

2 OBSERVATIONS

2.1 WISDOM sample

WISDOM ALMA data (with a typical resolution of $\approx 0''.1$ or 30 pc) were originally collected with the intent of measuring SMBH masses. The main selection criterion for WISDOM galaxies was thus to have the SMBH sphere of influence (SOI)[2] spatially-resolvable with ALMA. Therefore, our sample of galaxies is fairly heterogeneous, containing both nearly-quenched ETGs and star-forming spirals with a range of nuclear activities. In particular, here we study data of

---

[1] The Eddington ratio is a measure of the level of nuclear activity and is defined as $\lambda_{\rm Edd} = L_{\rm bol}/L_{\rm Edd}$, where $L_{\rm bol}$ is the AGN bolometric luminosity and $L_{\rm Edd} = 1.26 \times 10^{38} M_{\rm BH}$ erg s^{-1} is the Eddington luminosity.

[2] The SOI is the region where the gravitational potential of the SMBH dominates over that of the host galaxy and is defined as

$$R_{\rm SOI} \equiv G M_{\rm BH}/\sigma_*^2, \tag{1}$$

where $M_{\rm BH}$ is the mass of the SMBH, σ_* is the stellar velocity dispersion of the host bulge and G is the gravitational constant.

35 WISDOM objects, spanning stellar masses $M_\star$ from $10^{9.1}$ to $10^{11.8}$ M$_\odot$, and 1.4 GHz radio luminosities $L_{1.4\text{GHz}}$ from $\approx 10^{34}$ to $\approx 10^{41}$ ergs s^{-1}. The sample galaxies and their basic parameters are listed in Table 1. The AGN properties of our sample sources are discussed in detail below, and comparisons of these with other literature samples are presented in Section 4.1.

2.2 ALMA observations and data reduction

Thirty-two sample objects were observed in ^{12}CO(2-1) and 230 GHz continuum using ALMA Band 6, while three (NGC3351, NGC4429, NGC4826) have Band 7 ^{12}CO(3-2) and 345 GHz continuum observations. The ALMA observations used in this work were taken between 2013 and 2020 as part of a large number of projects (see Table 1). **For each target we used multiple ALMA observations with multiple array configurations. This enabled us to reach high angular resolution, while ensuring adequate uv-plane coverage and excellent flux recovery**. The spectral configuration always consisted of four spectral windows (SPWs), one centred on the redshifted frequency of the the ^{12}CO line (rest frequency 230.5 GHz for the 2–1 transition, 345.8 GHz for 3–2). The other three SPWs were used to observe the continuum. ALMA data were reduced using the Common Astronomy Software Applications (CASA) pipeline (McMullin et al. 2007) version appropriate for each dataset. A standard calibration strategy was adopted for every observation. A single bright object (typically a quasar) was used as both flux and bandpass calibrator, while a second bright object was used as a phase calibrator. More details on the data reduction process can be found in Davis et al. (2022).

2.2.1 Line imaging

In this work we make use of the CO data cubes presented in Davis et al. (2022), or used the same cleaning methods described therein **for consistency**. The final cleaned cubes have synthesised beam sizes ranging from 0″.054 to 0″.659, corresponding to spatial scales from 0.8 to 291 pc, and noise levels ranging from 0.19 mJy beam^{-1} to 3.70 mJy beam^{-1}. Since we are interested only in the gas reservoirs on scales $\lesssim$ 100 pc (i.e. those relevant for the SMBH accretion process), we restrict our analysis to the sub-sample of 29 WISDOM galaxies whose ALMA data cubes satisfy such spatial resolution requirement.

2.3 Ancillary Data

We gathered a variety of ancillary data to assess the level of nuclear activity in our targets and test its connection with the cold gas reservoirs observed with ALMA. For each source, we thus retrieved 2–10 keV X-ray, 1.4 GHz radio continuum and optical [OIII]λ5007 luminosities from the NASA Extragalactic Database (NED)[3] or other literature sources.

All the ancillary observations used in this work are listed in Table A1. In the following, we briefly describe each set of ancillary data and caveats around their use.

2.3.1 X-ray data

We retrieved the **nuclear 2–10 keV X-ray luminosities ($L_{X,2-10}$) of the majority of our sources from Bi et al. (2020), who presented a catalogue of nearby galaxies observed with *Chandra*. Ten sample**

---

[3] https://ned.ipac.caltech.edu/
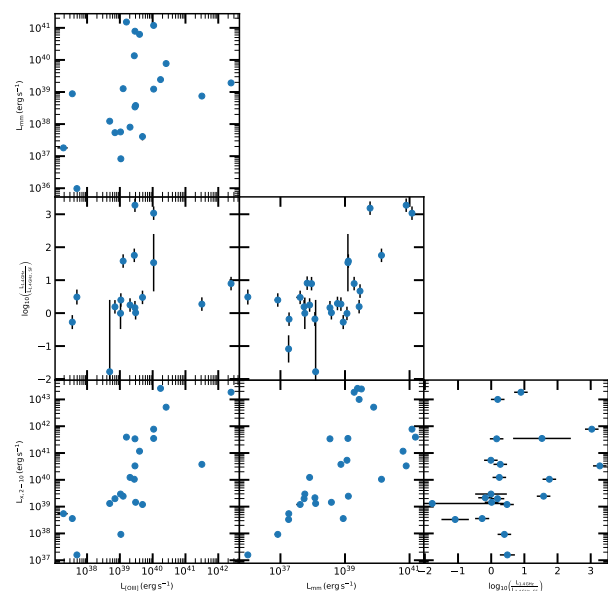
Figure 1. Correlations between the nuclear mm continuum luminosity, excess 1.4 GHz factor, 2–10 keV luminosity and the [OIII] luminosity. The Spearman rank coefficients and *p*-value of these correlations are listed in Table 3.

galaxies were not included in this catalogue[4], **thus their X-ray data were gathered from NED and come from a variety of satellites, i.e. Röntgensatellit (*ROSAT*), *EINSTEIN*, Advanced Satellite for Cosmology and Astrophysics (*ASCA*), XMM-*Newton* and *Chandra* (see Table A1). For four (NGC3351, NGC3862, NGC4429 and NGC4826) of these ten galaxies 2–10 keV luminosities were not available, thus we scaled the available measurement (0.2–2 keV for NGC3351 and NGC4429. 0.3–8 keV for NGC3862 and NGC4826) to the 2–10 keV energy band using a power law with an index −0.8 (corresponding to the mean reported by Reeves & Turner 2000). For eight sample galaxies X-ray data was not available.**

The 2–10 keV luminosities from Bi et al. (2020) include only nuclear emission from the unresolved AGN core. In the other ten cases, the spatial resolution of the available X-ray observations does not always allow to distinguish between nuclear AGN emission and other types of contribution on larger galaxy scales, thus possible sources of contamination need to be considered. Among these, there is emission from the diffuse hot atmospheres in and around galaxies (i.e. the circumgalactic medium, CGM). This low-surface brightness emission, however, usually requires very deep X-ray observations to be detected, and is typically dominant in the softer (0.3–2 keV) energy range. As such, we expect CGM contamination to be minimal even in low-resolution 2–10 keV X-ray data. A relatively larger contribution from the CGM may be present in faint X-ray sources and in the four cases in which the 2–10 keV luminosities where extrapolated from lower energy bands.

Stellar X-ray binaries are another potential source of contamination. **The K-band luminosity has been demonstrated to correlate with the luminosity of low mass X-ray binaries (LMXB). We thus use the K_s-band flux to estimate the contribution of LMXB to the 2–10 keV emission using the relations from Kim & Fabbiano (2004) and Boroson et al. (2011). We find that in three of the ten**

---

[4] FRL49, FRL1146, NGC0449,NGC0524, NGC1194, NGC3351, NGC3368, NGC3862, NGC4429 and NGC4826

Table 1. Physical parameters of the galaxies sample.

Galaxy	Distance (Mpc)	Jet	Galaxy type	AGN type	$\log(M_\star/M_\odot)$	Mass Ref	$\log(\mathrm{SFR}/M_\odot\,\mathrm{yr}^{-1})$	Project code	Reference
(1)	(2)	(3)	(4)	(5)	(6)	(7)	(8)	(9)	(10)
FRL49	85.7	No	E-S0	Seyfert 2	10.30	L22	0.78	b	Lelli et al. (2022)
FRL1146	136.7	Yes	Sc	Seyfert 1	11.32	M_{K_s}	-	a,b	This work
MRK567	140.6	No	Sc	-	11.26	C17	1.30	a,b	Davis et al. (2022)
NGC0383	66.6	Yes	E-S0	LERG	11.82	MASSIVE	0.00	c,d,e	North et al. (2019)
NGC0404	3.0	No	E-S0	LINER	9.10	S10	-3.04	f	Davis et al. (2020)
NGC0449	66.3	No	SBa	Seyfert 2	10.07	z0MGS	1.19	c,d	Davis et al. (2022)
NGC0524	23.3	No	S0-a	-	11.40	z0MGS	-0.56	e,g,h	Smith et al. (2019)
NGC0612	130.4	Yes	S0-a	LINER	11.76	M_{K_s}	0.85	b,j	Ruffa et al. (2023)
NGC0708	58.3	Yes	E	LERG	11.75	MASSIVE	-0.29	e,h,i	North et al. (2021)
NGC1194	53.2	No	S0-a	Seyfert 2	10.64	z0MGS	-1.74	j	This work
NGC1387	19.9	No	E-S0	LINER	10.67	z0MGS	-0.68	d,e	Boyce, in prep
NGC1574	19.3	No	E-S0	-	10.79	z0MGS	-0.91	c,e	Ruffa et al. (2023)
NGC2110	35.6	No	E-S0	-	10.41	M_{K_s}	-	c,k	This work
NGC3169	18.7	Yes	Sa	Seyfert 1	10.84	z0MGS	0.29	e,i	Davis et al. (2022)
NGC3351	10.0	Yes	Sb	LERG	10.28	z0MGS	-	e,o	This work
NGC3368	18.0	Yes	Sab	LERG	10.67	z0MGS	-0.29	k	Davis et al. (2022)
NGC3607	22.2	No	E-S0	-	11.34	A3D	-0.54	e,i	Davis et al. (2022)
NGC3862	92.5	Yes	E	LERG	11.68	MASSIVE	-	a,e,i,l	This work
NGC4061	94.1	Yes	E	-	11.54	MASSIVE	-0.71	a,e,i,l	Davis et al. (2022)
NGC4261	31.9	Yes	E	LINER	10.80	M_{K_s}	-	a,l	Ruffa et al. (2023)
NGC4429	16.5	No	S0-a	-	11.17	A3D	-0.84	e,o	Davis et al. (2018)
NGC4435	16.5	No	S0	-	10.69	A3D	-0.84	e,i	Davis et al. (2022)
NGC4438	16.5	No	Sa	LINER	10.75	z0MGS	-0.3	e,i	Davis et al. (2022)
NGC4501	14.0	Yes	Sb	Seyfert 2	11.00	z0MGS	0.43	e,m	Davis et al. (2022)
NGC4697	11.4	No	E	-	11.07	A3D	-1.08	i	Davis et al. (2017)
NGC4826	7.4	No	SABa	Seyfert 1	10.20	z0MGS	-0.71	e,o	Davis et al. (2022)
NGC5064	34.0	No	Sb	-	10.93	z0MGS	0.11	e,g	Davis et al. (2022)
NGC5765b	114.0	No	SABb	Seyfert 2	11.21	M_{K_s}	1.43	j	Davis et al. (2022)
NGC5806	21.4	Yes	Sb	Seyfert 2	10.57	z0MGS	-0.03	d,e	Davis et al. (2022)
NGC5995	107.5	No	SABa	Seyfert 2	11.41	M_{K_s}	-	b	This work
NGC6753	42.0	No	Sb	-	10.78	z0MGS	0.32	e,g	Davis et al. (2022)
NGC6958	30.6	No	E	-	10.76	z0MGS	-0.58	e,g	Thater, in prep
NGC7052	51.6	Yes	E	LERG[1]	11.75	MASSIVE	-0.07	a,l	Smith et al. (2021a)
NGC7172	33.9	No	Sa	Seyfert 2	10.76	z0MGS	0.38	n	Davis et al. (2022)
PGC043387	95.8	No	E	-	11.12	M_{K_s}	-0.48	i	This work

Notes: (1) galaxy name, (2) galaxy distance in Mpc, (3) whether a resolved radio jet is present in radio observations of the galaxy, (4) galaxy morphological type, (5) AGN type or HERG/LERG classification (determined using classification from Figure 2 of Best & Heckman 2012). The radio AGN classification of NGC7052 was taken from Gleisinger et al. (2020). (6) galaxy stellar mass, (7) the reference for the stellar mass: L22 refers Lelli et al. (2022), C17 refers to Cook et al. (2017), S10 refers to Seth et al. (2010), A3D refers to Cappellari et al. (2013), MASSIVE refers to Veale et al. (2017), and z0MGS to Leroy et al. (2019). M_{K_s} refers to masses estimated from the galaxies K_s-band magnitude using Equation 2 of Cappellari (2013). (8) the star formation rate of the galaxy. The uncertainties on the star formation rates are 0.2 dex for all sources except NGC0404, NGC1194 and PGC043387 which have uncertainties of 0.22, 0.87 and 0.22 dex respectively. (9) ALMA Project codes of each source, where a: 2016.2.00046.S, b: 2017.1.00904.S, c: 2015.1.00419.S, d: 2016.1.00437.S, e: 2016.2.00053.S, f: 2017.1.00572.S, g: 2015.1.00466.S, h: 2017.1.00391.S, i: 2015.1.00598.S, j: 2016.1.01553.S, k: 2016.1.00839.S, l: 2018.1.00397.S, m: 2015.1.00046.S, n: 2019.1.00363.S and o: 2013.1.00493. (10) reference where the ALMA data were initially presented.

galaxies for which data was not available from Bi et al. (2020) the contributions form LMXBs is minimal (<5%). In the other seven galaxies (NGC0449, NGC0524, NGC3351, NGC3368, NGC3862, NGC4429 and NGC4826) the contribution expected from LMXB is larger (>5%). To estimate the potential contamination from high mass X-ray binaries (HMXB) we used the relation between SFR and X-ray luminosity from Grimm et al. (2003). Again for the ten galaxies for which data was not available from Bi et al. (2020) we found two galaxies had minimal contributions (<5%), five galaxies (NGC0449, NGC0524, NGC3368, NGC4429 and NGC4826) had larger contributions (>5%), and three galaxies we did not have the SFRs so could not calculate the contributions from HMXB (FRL1146, NGC3351 and NGC3862). We therefore assume that the 2-10 keV luminosity of most of our targets is dominated by AGN emission from the core. In few individual

sources, however, it is possible that we slightly overestimate the AGN luminosity due to the aforementioned uncertainties.

2.3.2 Radio data

We used 1.4 GHz radio observations to probe the type of nuclear activity, and the presence of radio jets. The data used in this work are mostly from the Very Large Array sky surveys, such as the Faint Images of the Radio Sky at Twenty-Centimeters (FIRST; Becker et al. 1994), and the NRAO VLA Sky Survey (NVSS; Condon et al. 1998). The spatial resolution of these surveys is typically very poor (e.g. $45''$ for the NVSS). While this does not allow us to resolve nuclear radio structures, it does ensures that no radio emission is resolved out and that any associated large-scale radio jet is detected. For the one source (NGC1574) for which 1.4 GHz observations were not available, we scaled the available 5GHz radio

data to 1.4 GHz using a power law with a spectral index $\alpha = -0.8$ (for $S \propto \nu^{\alpha}$), as typical for optically-thin radio jet emission (e.g. Komissarov & Gubanov 1994; Laing & Bridle 2013).

It is possible that some of the radio emission detected in our targets is contaminated by star formation within the galaxy (e.g. from supernova remnants). To quantify such putative contribution, we gathered the star formation rates (SFRs) of our sample sources from Davis et al. (2022), when available. For the 6 sample galaxies not included in that work, we estimated the SFRs adopting the following relation:

$$\text{SFR} = \frac{M_{\text{H}_2}}{\tau} \tag{2}$$

where M_{H_2} is the total molecular gas mass withing the galaxy (calculated as described in Section 3.1), and τ is the depletion time, assumed to be 2 Gyr (e.g Leroy et al. 2008). We then estimated the expected 1.4 GHz radio luminosity due to star formation using the following relation (Murphy et al. 2011):

$$\left(\frac{\text{SFR}_{\nu}}{\text{M}_{\odot}\text{yr}^{-1}}\right) = 10^{-27}\left[2.18\left(\frac{T_e}{10^4\text{K}}\right)^{0.45}\left(\frac{\nu}{\text{GHz}}\right)^{-0.1} + 15.1\right.$$
$$\left.\left(\frac{\nu}{\text{GHz}}\right)^{\alpha^{\text{NT}}}\right]^{-1}\left(\frac{L_{\nu}}{\text{erg s}^{-1}\text{Hz}^{-1}}\right), \tag{3}$$

which can be rearranged to:

$$\left(\frac{L_{\nu}}{\text{erg s}^{-1}\text{Hz}^{-1}}\right) = 10^{27}\left(\frac{\text{SFR}_{\nu}}{\text{M}_{\odot}\text{yr}^{-1}}\right)\left[2.18\left(\frac{T_e}{10^4\text{K}}\right)^{0.45}\left(\frac{\nu}{\text{GHz}}\right)^{-0.1}\right.$$
$$\left. + 15.1\left(\frac{\nu}{\text{GHz}}\right)^{\alpha^{\text{NT}}}\right] \tag{4}$$

where ν is the observed frequency, T_e is the electron temperature and α^{NT} is the non-thermal spectral index. We assumed $T_e = 10^4$ K (Murphy et al. 2011) and $\alpha = -0.8$ (Murphy et al. 2011). The relation combines thermal radio emission (calculated from the ionizing photon production rate) and non-thermal radio emission from supernovae, both of which are related directly to the SFR.

From the ratio between the total radio luminosity and that expected from star formation, $\log_{10}(L_{1.4\text{GHz}}/L_{1.4\text{GHz,SF}})$, we calculate what we call the **the radio excess factor** ($E_{1.4}$). In galaxies with $E_{1.4}$ **significantly larger than zero**, the detected radio emission cannot be explained by star formation, and thus likely arises from nuclear activity. The radio excess factor for each galaxy is tabulated in Table A1.

2.3.3 Optical line data

[O III]λ5007 is typically the strongest emission line in optical spectra of AGN and arises from gas in the narrow line regions (NLRs) that has been photo-ionised by the AGN radiation. It is then usually considered as a good proxy of the AGN bolometric luminosity (e.g. Heckman & Best 2014). [O III] has also the advantage to be a more ubiquitous tracer of nuclear activity than the 2-10 keV luminosity, as it is observed in both kinetic- and radiative-mode AGN and does not suffer of any obscuration from the dusty torus (present in typical Seyfert-like objects). **We therefore collected [OIII]λ5007 luminosities from a variety of instruments/surveys, such as the double spectrograph at the** *Hale Telescope* **(Ho et al. 1995),** *El Leoncito Astronomical Complex* **(CASLEO; Bonatto & Pastoriza 1997; Rodríguez-Ardila et al. 2000), the DOLORES (Device Optimized for the LOw RESolution) spectrograph at** *Galileo National Telescope* **(TNG; Buttiglione et al. 2009),** *Sloan Digital Sky Survey* **(SDSS; Zhu et al. 2011),** *MPG/ESO telescope* **(Tadhunter et al. 1993), the spectrograph on the** *Shane Telescope* **at Lick Observatory (De Robertis & Osterbrock 1986; Crawford et al. 1999) and the** *CTIO Telescope* **(Moustakas et al. 2010). Where available, we additionally gather Hβ luminosities from the same archives. These are useful to calculate the [OIII]/Hβ ratio and thus to assess the dominant line excitation mechanism (e.g. Baldwin et al. 1981). 15 sample galaxies had both [OIII]λ5007 and Hβ data available. We find that the [OIII]/Hβ ratio of these sources ranges from 0.16 to 5.13, with only 5 objects (FRL1146, NGC0524, NGC3351, NGC4429 and NGC4435) having ratios lower then one (i.e. SF-dominated galaxies). In all the other cases, the ratios are > 1, as typical in AGN-dominated objects.**

We note that the [OIII]λ5007 line may be contaminated by star formation or old stars, or be affected by extinction arising within the host galaxy. However, star formation is only expected to contribute significantly in higher-redshift galaxies (whereas it should be negligible in nearby objects such as our sample sources; Suzuki et al. 2016).

2.3.4 ALMA nuclear continuum emission

We gathered the ALMA nuclear continuum luminosities and the associated (in-band) nuclear mm spectral indices from Ruffa et al. (submitted). The mm continuum emission was measured from the brightest central pixel in the ALMA continuum map of each galaxy.

2.3.5 Accretion tracer correlations

The correlations between the nuclear mm luminosity, X-ray luminosity, [OIII] luminosity and excess radio factor are shown in Figure 1, with the correlation coefficients and p-values listed in Table 3. This figure shows that the four tracers of activity mostly correlate with each other despite different contaminants, suggesting we are tracing nuclear activity rather then larger scale emission. This also shows that, even though some of the galaxies in our sample are not formally classified as AGN, low-level nuclear activity seems to be present.

2.3.6 Stellar masses

The stellar masses of the majority of our sample galaxies were taken from Davis et al. (2022), who in turn collected them from the ATLAS$^{\text{3D}}$ (Cappellari et al. 2013) and MASSIVE (Veale et al. 2017) surveys, and the z=0 Multiwavelength Galaxy Synthesis (z0MGS) project (Leroy et al. 2019). The stellar masses for MRK 567 and NGC 0404 were taken from Cook et al. (2017) and Seth et al. (2010), respectively. Where stellar mass measurements were not available in the literature, we estimated them from the K_s-band magnitudes measured in the **extended source catalogue** of the 2 micron All-Sky Survey (2MASS; Jarrett et al. 2003). We used Equation 2 of Cappellari (2013), with no correction for the emission from the AGN (as this should be small at these frequencies in our low-luminosity sources):

$$\log_{10}M_* \approx 10.58 - 0.44 \times (M_{K_s} + 23) \tag{5}$$

where M_* is the stellar mass and M_{K_s} is the K_s-band magnitude.

3 METHODOLOGY AND DERIVED QUANTITIES

In this work we search for correlations between *circumnuclear* molecular gas reservoirs and SMBH fuelling across a sample of galaxies with a range of nuclear activities. This requires us to assess both the amount of molecular gas present in the circumnuclear regions, and its structure. Furthermore, we need to constrain the SMBH accretion rate in our sources, and the type of nuclear activity. Below we describe the methodology we adopted to determine these quantities.

3.1 Molecular gas masses

We adopt the following relation to estimate the molecular hydrogen gas masses (M_{H_2}) of our galaxies within different apertures (Bolatto et al. 2013):

$$M_{H_2} = 2m_H \frac{\lambda^2}{2k_B} X_{CO} D_L^2 R \int S_\nu \, dV, \tag{6}$$

where m_H is the mass of the hydrogen atom, λ is the rest wavelength of the observed molecular transition, k_B is the Boltzmann constant, X_{CO} is the CO-to-H_2 conversion factor, D_L is the luminosity distance, $R \equiv T_{b,ref}/T_{b,CO(1-0)}$ is the line intensity ratio (i.e. the ratio between the ground state and the observed CO line brightness temperature), and $\int S_\nu dV$ is the integrated flux density of the CO(1-0) line, with units matching those of X_{CO}. This was estimated by integrating the spectrum of the observed CO transition within a given aperture over all the velocity channels of the line. Equation 6 can be simplified to

$$\left(\frac{M_{H_2}}{M_\odot}\right) = 7847 \, J_{upper}^{-2} X_{CO,2\times10^{20}} R \left(\frac{D_L}{Mpc}\right)^2 \left(\frac{\int S_v dV}{Jy \, kms^{-1}}\right), \tag{7}$$

where J_{upper} is the upper state rotational quantum number of the observed transition (here J_{upper} is 2 or 3) and $X_{CO,2\times10^{20}} = \frac{X_{CO}}{2\times10^{20} \, cm^{-2}(K \, km \, s^{-1})^{-1}}$. As most of our galaxies are massive and metal-rich, we assume a Milky Way-like CO-to-H_2 conversion factor of $3 \times 10^{20} cm^{-2}(K \, km \, s^{-1})^{-1}$ (Strong et al. 1988). We also assume the line ratios to be $T_{b,CO(2-1)}/T_{b,CO(1-0)} = 0.7$ and $T_{b,CO(3-2)}/T_{b,CO(1-0)} = 0.3$ (see e.g. Leroy et al. 2022). For sample galaxies observed with ALMA at adequate spatial resolutions, we estimated the molecular gas mass within three different elliptical apertures of radii 100, 75, and 50 pc. We additionally measure the molecular gas mass in a elliptical aperture with a radius of 200 pc to measure the nuclear molecular gas concentration. The resulting M_{H_2} are listed in Table 2. As mentioned above, the molecular gas masses were all calculated with a fixed X_{CO} factor. We note, however, that the CO-to-H_2 conversion factors in galaxy centres may vary (Sandstrom et al. 2013), adding uncertainty at a ~0.3 dex level. To aid comparisons with different X_{CO} prescriptions, we provide the CO integrated flux densities measured within the different apertures in Table A3. We assume an additional 10% error on our molecular gas masses due to ALMA calibration uncertainties.

To assess the structure of the molecular gas at the centre of each sample galaxy, following García-Burillo et al. (2021), we also calculated the molecular concentration parameter:

$$\frac{\Sigma_{H_2}^{50pc}}{\Sigma_{H_2}^{200pc}} = 16 \left(\frac{M_{H_2}^{50pc}}{M_{H_2}^{200pc}}\right), \tag{8}$$

where $\Sigma_{H_2}^{xpc}$ and $M_{H_2}^{xpc}$ are the molecular gas surface density and mass, respectively, within a elliptical aperture of radius x pc. We assumed that the gas lies within a flat disc so $\Sigma_{H_2}^{xpc} = \frac{M_{H_2}^{xpc}}{\pi x^2}$.

3.2 Accretion rates

To estimate the SMBH accretion rates in each source, we use the following relation (Alexander & Hickox 2012):

$$\left(\frac{\dot{M}_{BH}}{M_\odot \, yr^{-1}}\right) = 0.15 \left(\frac{0.1}{\eta}\right) \left(\frac{L_{Bol}}{10^{45} \, ergs \, s^{-1}}\right) \tag{9}$$

where L_{Bol} is the AGN bolometric luminosity and η is the mass-energy conversion efficiency factor, typically assumed to be 0.1 (e.g. Marconi et al. 2004).

We follow two prescriptions to estimate the AGN bolometric luminosities. The 2–10 keV X-ray luminosity is generally considered a good proxy of the AGN bolometric luminosity in radiative-mode AGN (e.g. Ho 2008), and can be calculated inverting the bolometric correction relation of Marconi et al. (2004):

$$\log_{10}\left(\frac{L_{Bol}}{L_{2-10keV}}\right) = 1.54 + 0.24\mathcal{L} + 0.012\mathcal{L}^2 - 0.0015\mathcal{L}^3, \tag{10}$$

where $\mathcal{L} \equiv \log_{10}\left(\frac{L_{Bol}}{L_\odot}\right) - 12$.

In kinetic-mode AGN, the 2–10 keV emission may instead arise from inverse Compton up-scattering of non-thermal photons from the radio jet (e.g. Blundell et al. 2006). For this reason, we additionally used the [OIII]λ5007 luminosity as a proxy of L_{Bol}, adopting the bolometric correction $L_{bol}/L_{[OIII]} \approx 3500$ (Heckman et al. 2004). **As illustrated in Table 1, a clear AGN classification is missing for some of our sample galaxies (13/35), whereas the majority of them consist on a mix of radiative- and kinetic-mode AGN. For each source, we thus calculate L_{bol} using both the 2–10 keV and [OIII]λ5007 luminosity as tracers. We show the relation between these two derived bolometric luminosities in Figure A1.**

4 RESULTS AND ANALYSIS

4.1 Properties of WISDOM AGN

As discussed above, in this work we aim to investigate previous claims that at circumnuclear scales (<100 pc) accretion rate tracers should correlate with the mass and structure of the cold molecular gas mass. **As illustrated in Table 1, our sample consists on systems with a diverse range of nuclear activities. In order to further place the WISDOM galaxies in context with previous studies, in Figure 2 we illustrate the main properties of the AGN in our sample (i.e. bolometric luminosity, black hole mass, Eddington ratio, central velocity dispersion and jet power), compared with those from the works of Izumi et al. (2016), Babyk et al. (2019) and García-Burillo et al. (2021) with the medians for the samples used and the KS test p-values between the sample are shown in Table A4.**

It is clear from Figure 2 that the bolometric luminosities of our AGN are consistent with those of the samples studied by Izumi et al. (2016) and García-Burillo et al. (2021), and we probe a range of radio jet powers similar to that of the sources analysed by Babyk et al. (2019). On the other hand, the SMBH masses of the AGN in our sample are larger - on average - than those probed in such previous studies, and thus their Eddington ratios are slightly lower (at least when compared with the work of Izumi et al. 2016).

More generally, Figure 2 shows that there is overlap between the main properties of the AGN in our sample and those in the previous reference studies, with the WISDOM objects being also clearly complementary to such works. In the following, we will

Table 2. Circumnuclear masses for different region sizes and millimetre spectral indices for our sources.

Galaxy	$\log\left(\frac{M_{H_2}}{M_\odot}\right)$	$\Delta \log M_{H_2}$	$\log\left(\frac{M_{H_2}}{M_\odot}\right)$	$\Delta \log M_{H_2}$	$\log\left(\frac{M_{H_2}}{M_\odot}\right)$	$\Delta \log M_{H_2}$	$\log\left(\frac{M_{H_2}}{M_\odot}\right)$	$\Delta \log M_{H_2}$	$S_{\nu,mm}$	$\sigma S_{\nu,mm}$
	(200 pc)		(100 pc)		(75 pc)		(50 pc)			
		(dex)		(dex)		(dex)		(dex)	(mJy)	(mJy)
(1)	(2)	(3)	(4)	(5)	(6)	(7)	(8)	(9)	(10)	(11)
FRL49	8.34	0.04	7.87	0.04	-	-	-	-	0.93	0.038
FRL1146	-	-	-	-	-	-	-	-	0.47	0.0272
MRK567	8.90	0.04	8.52	0.04	-	-	-	-	<0.11	0.0354
NGC0383	8.15	0.04	7.71	0.04	7.48	0.04	7.08	0.04	63	0.101
NGC0404	6.18	0.04	6.18	0.04	6.17	0.04	6.14	0.04	0.38	0.012
NGC0449	-	-	-	-	-	-	-	-	0.60	0.0246
NGC0524	7.42	0.04	6.93	0.05	6.75	0.04	6.47	0.04	5.7	0.023
NGC0612	8.20	0.04	7.62	0.04	7.50	0.04	7.35	0.05	25	0.06
NGC0708	8.12	0.04	7.66	0.04	7.47	0.04	7.13	0.05	1.3	0.0165
NGC1194	7.48	0.04	7.13	0.04	6.95	0.05	-	-	1.6	0.0286
NGC1387	7.66	0.04	7.05	0.04	6.80	0.04	6.43	0.04	1.0	0.0535
NGC1574	6.79	0.04	6.74	0.04	6.66	0.04	6.40	0.04	3.3	0.033
NGC2110	7.35	0.04	6.77	0.04	-	-	-	-	21	0.453
NGC3169	8.26	0.04	7.80	0.04	7.60	0.04	-	-	3.4	0.107
NGC3351	7.66	0.04	7.39	0.04	7.16	0.04	6.91	0.04	<0.45	0.148
NGC3368	8.36	0.04	7.87	0.04	7.68	0.05	7.42	0.04	<0.56	0.202
NGC3607	7.89	0.04	7.51	0.04	7.33	0.04	-	-	2.7	0.164
NGC3862	-	-	-	-	-	-	-	-	64	1.43
NGC4061	7.65	0.04	7.10	0.04	6.90	0.04	-	-	2.4	0.18
NGC4261	7.32	0.04	7.29	0.04	7.21	0.04	7.02	0.04	220	1.53
NGC4429	7.31	0.04	6.64	0.04	6.38	0.04	5.88	0.04	1.1	0.0853
NGC4435	7.61	0.04	7.25	0.04	7.05	0.05	6.78	0.04	0.73	0.0246
NGC4438	8.19	0.04	7.78	0.04	7.58	0.04	7.24	0.04	0.52	0.126
NGC4501	8.06	0.04	7.72	0.04	7.52	0.05	7.22	0.04	1.4	0.0789
NGC4697	6.02	0.04	5.93	0.04	5.83	0.04	5.61	0.04	0.48	0.0444
NGC4826	8.16	0.04	8.01	0.04	7.90	0.04	7.60	0.04	0.38	0.0746
NGC5064	8.13	0.04	7.67	0.04	7.41	0.04	7.10	0.04	0.28	0.0259
NGC5765b	8.41	0.04	-	-	-	-	-	-	0.328	0.0616
NGC5806	7.57	0.04	7.16	0.04	7.02	0.04	6.77	0.05	<0.14	0.0473
NGC5995	-	-	-	-	-	-	-	-	0.99	0.0331
NGC6753	8.63	0.04	8.16	0.05	7.94	0.04	7.62	0.04	<0.14	0.0447
NGC6958	7.70	0.04	7.17	0.04	6.96	0.04	6.61	0.04	11	0.0569
NGC7052	7.75	0.04	7.39	0.04	7.17	0.04	6.79	0.04	18	0.0823
NGC7172	8.36	0.04	7.48	0.04	7.14	0.04	6.74	0.04	8.4	0.32
PGC043387	-	-	-	-	-	-	-	-	<0.31	0.104

Notes: (1) galaxy name. (2) mass measured within a elliptical aperture of 200 pc radius, with its uncertainty in (3). (4)-(9) follow the same pattern, for 100, 75 and 50 pc apertures. (10) nuclear mm continuum flux derived from all our ALMA data (fluxes measured separately from the lower and upper sidebands in Table A), (11) nuclear mm continuum flux uncertainty.

further discuss potential differences and if/how these may affect our results.

4.2 AGN luminosity – molecular gas mass correlations

In Figures 3-5 we show the obtained circumnuclear H_2 masses plotted against excess 1.4 GHz continuum, 2-10 keV X-ray and nuclear mm-continuum luminosity, respectively. To check for the statistical significance of such relations, we carried out a Spearman rank analysis, where we consider relations with p-values $\lesssim 0.05$ as statistically significant. The resulting Spearman rank coefficients and p-values are presented in Table 3

4.2.1 Excess radio luminosity– molecular mass correlation

We show in Figure 3 the correlation between molecular gas mass on sub-kpc scales and excess radio emission. There is no strong correlation between these quantities, as indicated by Spearman rank analysis (reported in the first row of Table 3). The correlation coefficient is

0.31 for the 100 pc radius aperture, and increases to 0.35 for the 75 pc and 0.55 for the 50 pc radius aperture, with p-values of 0.13, 0.10 and 0.01, respectively. We note that, based on these results, a mild correlation may be present at the 50 pc scale. However, we checked that this is driven by galaxies that are dominated by star formation. When these objects are excluded, the Spearman rank coefficient becomes -0.07, with a p-value of 0.82, thus excluding the presence of a correlation.

4.2.2 X-ray luminosity-molecular gas mass correlation

We show in Figure 4 the relation between the molecular gas mass on sub-kiloparsec scales and 2-10 keV X-ray luminosity. Also in this case, there is no correlation between the two quantities within any aperture size, as supported by the Spearman rank analysis (reported in the second row of Table 3). The correlation coefficients are 0.23 with a p-value of 0.30 for the case of the molecular gas mass calculated within a 100 pc radius aperture, 0.25 with a p-value of 0.29 for the

Table 3. Spearman rank coefficients and *p*-values

	Mass–Luminosity Correlations					
	$\log(M_{H_2,100pc}/M_\odot)$ (1)		$\log(M_{H_2,75pc}/M_\odot)$ (2)		$\log(M_{H_2,50pc}/M_\odot)$ (3)	
	Coefficient	*p*-value	Coefficient	*p*-value	Coefficient	*p*-value
$\log(E_{1.4})$	0.31	0.13	0.35	0.10	0.55	0.01
$\log(L_{X-ray,2-10})$	0.23	0.30	0.25	0.29	0.24	0.35
$\log(L_{mm})$	0.04	0.84	0.12	0.60	0.08	0.74
$\log(\dot{M}_{acc,X-ray})$	0.23	0.30	0.25	0.29	0.24	0.35
$\log(\dot{M}_{acc,[OIII]})$	0.22	0.36	0.35	0.16	0.51	0.06
	Luminosity–Luminosity Correlations					
	Coefficient			*p*-value		
	(4)					
$L_{mm}-L_{X-ray,2-10}$	0.76			3.37E-6		
$L_{mm}-E_{1.4}$	0.57			0.008		
$E_{1.4}-L_{X-ray,2-10}$	0.16			0.56		
$L_{[OIII]}-L_{X-ray,2-10}$	0.78			2.27E-5		
$L_{[OIII]}-E_{1.4}$	0.15			0.60		
$L_{[OIII]}-L_{mm}$	0.52			0.01		

Notes: (1) Spearman rank correlation coefficients and *p*-value for the 100 pc radius aperture, (2) and (3) same quantities for the 75 and 50 pc radius apertures. (4) lists the Spearman rank correlation coefficients and *p*-values between the luminosities studied.

75 pc radius aperture, and 0.24 with a *p*-value of 0.35 for the 50 pc radius aperture.

4.2.3 mm continuum luminosity– molecular gas mass correlation

The nuclear millimetre continuum luminosity is another proxy of the nuclear activity. Indeed, excess mm luminosity has been observed in AGN hosting galaxies, with the excess being **attributed to the AGN itself** (e.g. Behar et al. 2015, 2018; Doi & Inoue 2016; Wu et al. 2018; Kawamuro et al. 2022). We show in Figure 5 the **total nuclear millimetre luminosity** (calculated on scales $\lesssim 200$ pc) against the molecular gas mass on sub-kiloparsec scales, again finding no correlation between the two. The lack of correlation is supported by the Spearman rank analysis (reported in the third row of Table 3). The correlation coefficients are 0.04, 0.12 and 0.08 with *p*-values 0.84, 0.60 and 0.74 for the 100 pc, 75 pc and 50 pc regions, respectively.

4.3 Accretion rate–mass correlation

In Figures 6 and 7 we investigate relations between the molecular gas mass and AGN accretion rate, as calculated using the 2-10 keV and [OIII] line luminosity proxies. Also in this case, we do not find any clear correlation. The corresponding Spearman rank analysis (reported in the fourth and fifth rows of Table 3) mostly confirms this scenario.

For accretion rates calculated using the 2-10 keV luminosity as a proxy, a Spearman rank correlation coefficient of 0.23 with a *p*-value of 0.30 is obtained for the 100 pc radius aperture. For the 75 and 50 pc regions, the Spearman rank coefficients are 0.25 and 0.24, respectively, with associated *p*-values of 0.29 and 0.35.

For accretion rates calculated using the [OIII] line luminosity as a proxy, the Spearman rank coefficients are 0.22, 0.35 and 0.51 with p-values of 0.36, 0.16 and 0.06 for the 100 pc, 75 pc and 50 pc regions, respectively. These values imply that - as the aperture size decreases - a mildly significant correlation seems to be present. Whether this is real or coincidental due to the reduced number of data points should be investigated further.

5 DISCUSSION

### 5.1 AGN activity and the circumnuclear molecular gas

As described above, we do not find any strong correlation between the masses of molecular gas in the nuclear regions of our diverse sample galaxies and their AGN activities, as traced in a variety of ways. This is despite multiple authors reporting such correlations when studying specific AGN-selected samples of galaxies (e.g Izumi et al. 2016; Babyk et al. 2019). Our galaxies were not selected to be AGN, but do cover similar ranges of AGN properties (see Figure 2).

Our results suggests that the level of nuclear activity in a given galaxy cannot purely depend on the amount of cold gas around its SMBH. **This supports a recent work by Molina et al. (2023), where no correlation between the CO(2-1) and AGN luminosity has been reported**. In this work Molina et al. (2023) looked at the correlations between the cold molecular gas mass and AGN properties in a sample of Type 1 AGN at z$\lesssim$0.5. In this work the 5100Å AGN luminosity was used as analogy for the AGN bolometric luminosity. In Molina et al. (2023) they intially find a weak correlation between CO(2-1) and AGN luminosity but finds this disappears when correcting for the cosmic evolution of the molecular gas content in galaxies. This also clearly highlights that the SMBH fuelling mechanisms, that drives gas from the wider galaxy to the nuclear regions, are likely to be different in different types of AGN, and that timescale variations may be important. Below we discuss each of our tracers, and the conclusions that can be drawn from the differences between our results and others in literature.

5.1.1 X-ray emission

As described in Sections 4.2.2 and 4.3 (and illustrated in Figures 4 and 6, respectively), there is no correlation between the cold molecular gas masses in the circumnuclear regions and the X-ray luminosities/X-ray derived accretion rates of our sample galaxies. This is in contrast to Izumi et al. (2016), who reported a positive correlation between the dense ($n_{H_2} \gtrsim 10^{4-5} cm^{-3}$) molecular gas mass at ≈ 100 pc scales and the X-ray traced accretion rates (calculated using the same methods adopted here) onto the SMBHs of a
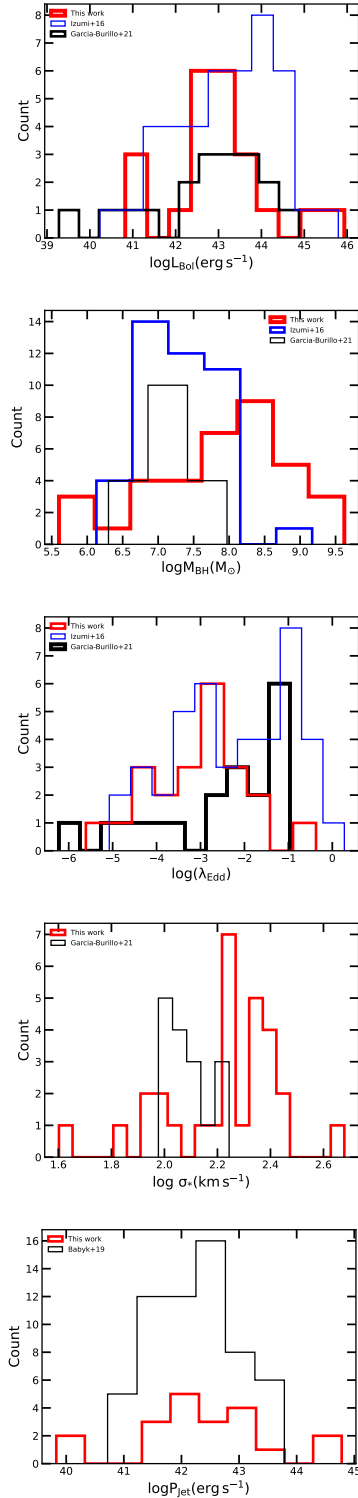
Figure 2. Distribution of AGN bolometric luminosity (top), black hole mass M_{BH} (second), Eddington ratio $\lambda_{\rm Edd}$ (third), velocity dispersion (fourth), and jet power (bottom) of the WISDOM sample. These are compared with the properties of the AGN from the works of Izumi et al. (2016), Babyk et al. (2019) and García-Burillo et al. (2021) which are discussed further in the text.

small sample of 10 nearby Seyfert galaxies. This was interpreted as supporting the role of CNDs in the AGN fuelling.

Differences between their results and ours may arise for several reasons. Firstly, Izumi et al. (2016) investigated the correlation between dense molecular gas mass of the CND and accretion rate only in ten Seyfert galaxies, whereas we consider a > 3 times larger sample of galaxies with a varied range of nuclear activities (see Figure 2) and AGN types (see Table 1). However, even when considering only the Seyferts in our sample, our results remain unchanged.

Another possibility to explain the lack of correlation is that different mechanisms usually give rise to the observed X-ray emission in different AGN types. In radiative-mode AGN such as Seyferts, X-rays are typically produced by inverse Compton up-scattering of photons from the accretion disk by the corona (Ciotti & Ostriker 1997). Whilst, in kinetic-mode AGN, classic accretion discs are either not present or truncated at inner radii (see Section 1), and X-ray emission likely arises from other processes, such as Compton up-scattering of non-thermal photons from the radio jets (e.g. Blundell et al. 2006). These two emission processes may not correlate directly or may differ in how they correlate with the cold molecular gas mass of the circumnuclear regions.

Furthermore, the correlation reported by Izumi et al. (2016) involves the dense ($n_{\rm H_2} \gtrsim 10^{4-5}{\rm cm}^{-3}$) molecular gas mass of the CNDs, estimated using the HCN molecule as tracer. Here we instead use the *total* molecular gas mass on circumnuclear scales, which has been estimated via CO emission. However, we still cannot make the Seyfert galaxies in our sample follow the correlation of Izumi et al. (2016) without requiring extremely low dense-gas fractions that also vary wildly between galaxies, a behaviour currently not observed in these kind of objects (e.g. Jiménez-Donaire et al. 2019).

Finally, it is widely believed that in radiative-mode AGN X-ray emission traces recently accreted material, as in these cases X-rays are expected to be produced very close to the central SMBH (e.g. Galeev et al. 1979). In this scenario, X-ray emission can be highly time-variable. However, it would take dynamical timescales of several hundred thousand years for the gas at the scales we are investigating to fall onto the SMBHs. This difference of timescales could also explain why we do not observed any correlation between the molecular gas mass in the circumnuclear regions and the 2-10 keV luminosity/X-ray traced accretion rate.

It is interesting to note that similar results have been also found in some recent works, looking at the correlation between the 2–10 keV X-ray luminosity and the CO(2-1) brightness (Rosario et al. 2018) or the molecular gas mass on kpc scales (García-Burillo et al. 2021) in small nearby samples of Seyfert galaxies. In both cases, the lack of correlation has been explained as being due to the difference in spatial scales and timescales between the X-ray emission and the molecular gas reservoirs. We thus speculate that the Seyfert galaxies observed by Izumi et al. (2016) may have been caught in a special phase with bright HCN emission, possibly suggesting a bias in the sample selection. Such bright HCN emission may be more common in Seyferts with sizeable dense molecular gas reservoirs, leading also to higher accretion rates than most of those probed by our sample. Further investigation of diverse galaxy samples in central regions < 50 pc in radius and using denser gas tracers will allow us to confirm/discard our hypothesis.

We finally note that the lack of correlation may be also ascribed to contamination from other (unresolved) sources of X-ray luminosity in the galaxies, such as stellar X-ray binaries (see Section 2.3.1). However, even when restricting our analysis only to sources observed at high spatial resolution with *Chandra*
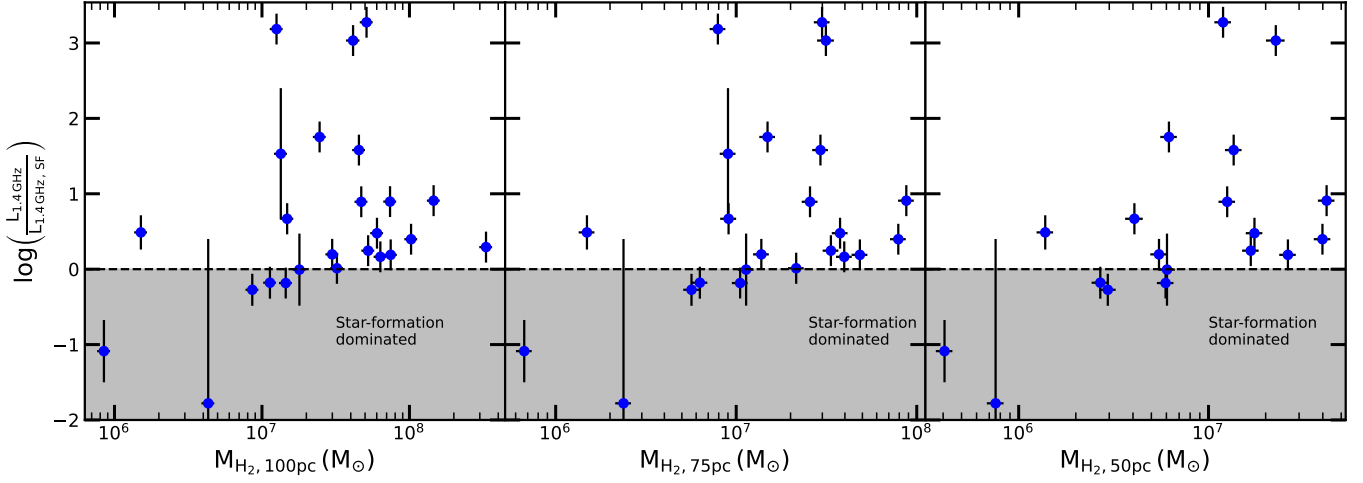
Figure 3. Molecular gas mass within an aperture of a given radius (100, 75 and 50 pc, as indicated by the x-axis labels) versus excess 1.4 GHz radio continuum fraction (after the contribution from star formation has been removed).
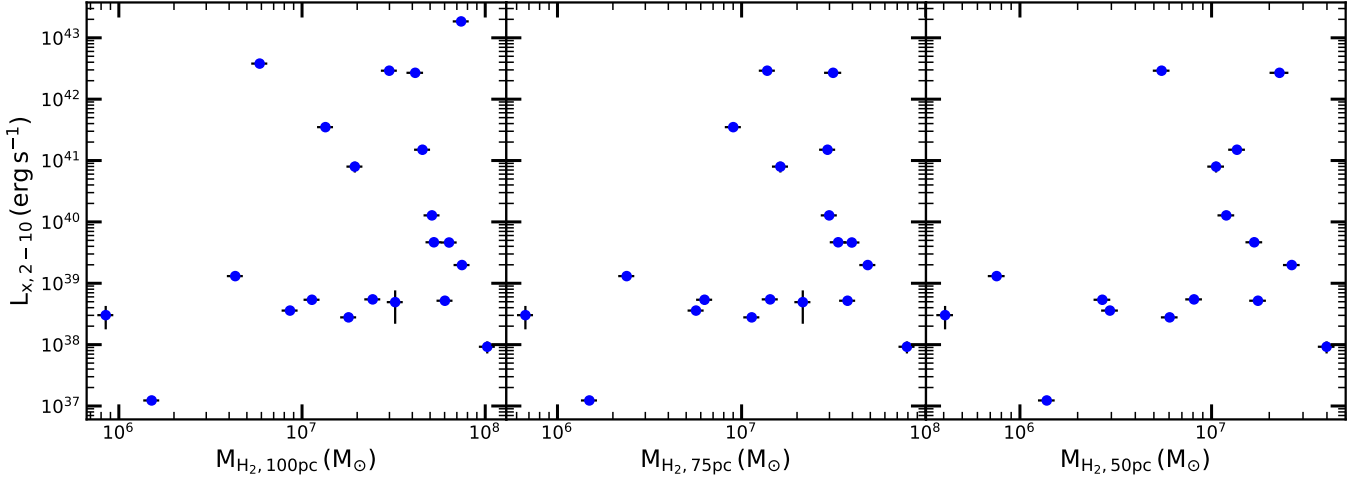
Figure 4. As Figure 3, but for the 2–10 keV X-ray luminosity.

(i.e. where the nuclear emission from the AGN can be spatially isolated), we still do not observe any correlation. This suggests that contamination is not driving our results.

5.1.2 Radio emission

Babyk et al. (2019) reported a relatively strong correlation between the molecular gas mass up to kpc scales and jet power in a sample of nearby ETGs, most of which are LERGs. We wanted to expand this study probing the gas mass down to circumnuclear scales and in a more diverse sample of galaxies. Babyk et al. (2019) calculated the radio power using the relation

$$P_{\nu_0} = 4\pi D_{\rm L}^2 (1+z)^{\alpha-1} S_{\nu_0} \nu_0 \qquad (11)$$

then calculated the radio jet power using this relation from Cavagnolo et al. (2010)

$$\log P_{\rm cav} = 0.75 \log P_{1.4} + 1.91. \qquad (12)$$

If the results reported by Babyk et al. (2019) held at circumnuclear scales, we would have expected to observe at least some correlation between the circumnuclear gas masses of our sample galaxies and the excess 1.4 GHz radio luminosities (as $P_{\rm jet} \propto L_{1.4}$; e.g. Cavagnolo et al. 2010). As discussed in Section 4.2.1 and illustrated in Figure 3, we do not find any sign of such correlation in this work. This could be explained if the correlation reported by Babyk et al. (2019) does not arise due to AGN fuelling processes, but because more massive galaxies tend to have more massive SMBHs, thus producing higher-power radio jets (Liu et al. 2006). **We note that a result similar to that of Babyk et al. (2019) has been recently reported by Fujita et al. (2023), who studied the correlation between the jet power estimated from X-ray cavities ($P_{\rm cav}$) and the molecular gas mass within 500 pc in a sample of 9 massive elliptical galaxies.**

Overall, the lack of correlation between the circumnuclear molecular gas mass and radio emission in our sample may suggest that jets are not directly powered by accretion from circumnuclear gas reservoirs, or that such correlation only exists over very long timescales.
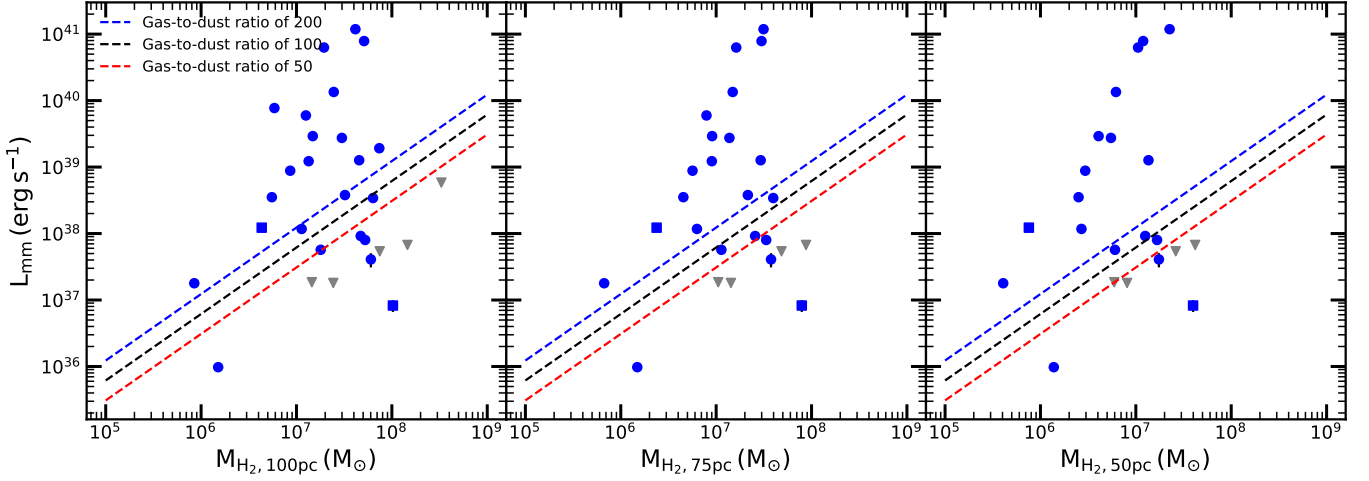
Figure 5. As Figure 3, but for the nuclear mm-continuum luminosity. Grey triangles are used for the upper limits (calculated as three times the rms noise level) of galaxies undetected in the mm continuum.
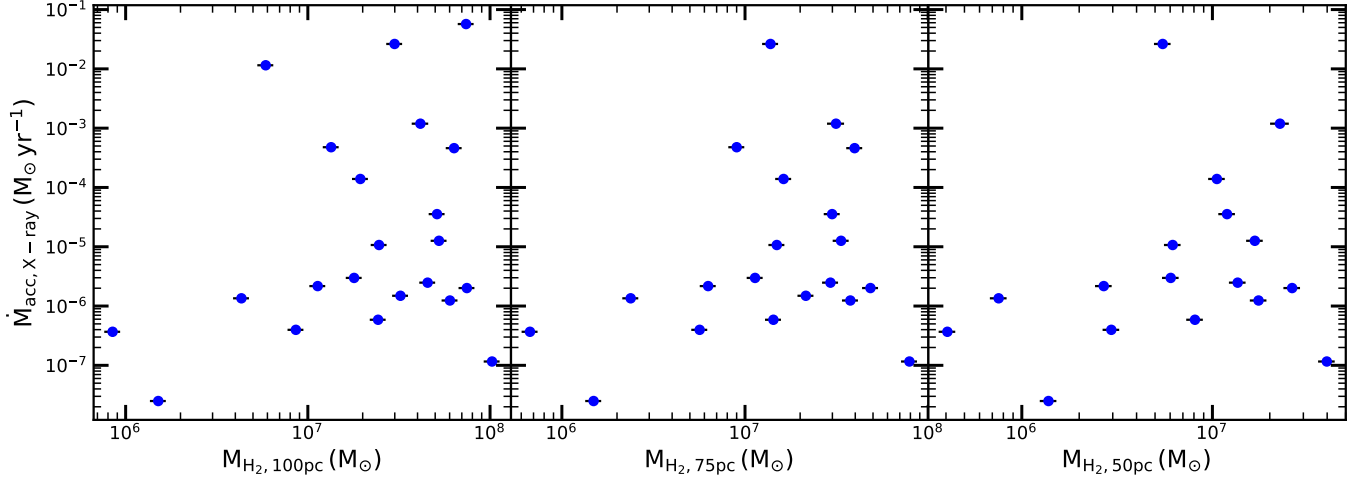
Figure 6. As Figure 3, but for the X-ray-traced accretion rate.

As discussed above, the dynamical times at the spatial scales probed here are still long compared to most AGN lifetime estimates. While radio jets can extend on large scales (and thus allow us to average AGN activity over longer timescales than direct tracers such as X-ray emission), this timescale mismatch may be too large to lead to any strong correlation.

5.1.3 Optical line emission

As described in Section 2.3.3, we estimated the accretion rate in our sources using also the [OIII] line emission as a tracer, finding again no correlation with the molecular gas mass in the circumnuclear regions (see Section 4.3 and Figure 7). One could ascribe this lack of correlation to contamination from other sources of [OIII] emission on larger scales (e.g. [OIII] can also be a tracer of star-forming regions). This kind of contamination, however, has been found to be relevant only in higher redshift galaxies (e.g. Suzuki et al. 2016), and should therefore be minimal in nearby galaxies like our sample sources.

This result provides support to the hypotheses formulated above that either the level of nuclear activity in a given galaxy does not exclusively depend on the amount of cold gas around the central SMBH, or temporal variations in the accretion rate wash out any correlation. These results also support the idea that AGN fuelling mechanisms are not ubiquitous and different processes may be at play in different AGN types.

5.2 Nuclear activity and structure of the molecular gas reservoir

For a sample of nearby Seyfert galaxies, García-Burillo et al. (2021) reported that AGN luminosity (traced by 2-10 keV X-ray emission) correlates strongly with the structure of the molecular ISM (traced by CO) in the central 200 pc. This could be due to AGN feedback impacting the cold molecular gas reservoirs at these scales, and driving the molecular gas away from (and/or heating/destroying it in) the centres of the galaxies.
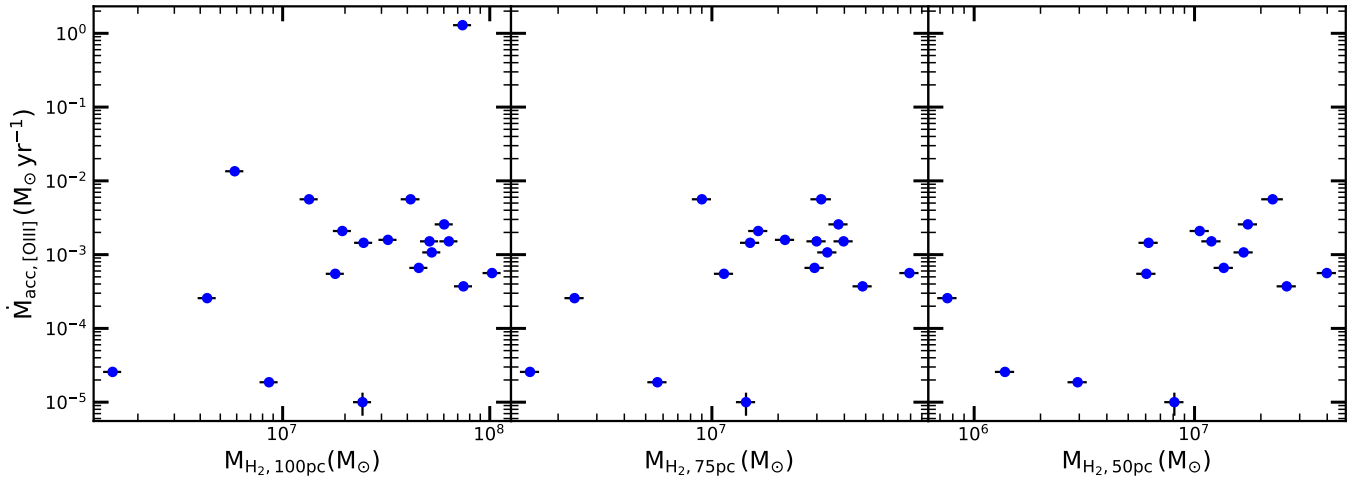
Figure 7. As Figure 3, but for the [OIII]-traced accretion rate.

As discussed in - e.g. - Davis et al. (2018), some of the WISDOM sample galaxies have central molecular gas holes, and so it is possible the same issue is occurring here. We test this in Figure 8, where we plot 2–10 keV X-ray luminosity against molecular gas concentration (as defined in Section 2) for both our sample and that of García-Burillo et al. (2021). Our galaxies span a range of X-ray luminosities and molecular gas concentrations similar to those of García-Burillo et al. (2021), but do not seem to follow the same correlation.

The lack of any correlation in our galaxy sample, which spans a wide range of AGN types and L_{bol} (10^{41} – 10^{46} erg s^{-1}) and does include a significant number of Seyferts (albeit not selected to be especially active), suggests two possibilities:

(i) The central structure of the molecular gas in galaxies is set by secular (non AGN-driven) process(es). The correlation of García-Burillo et al. (2021) could then arise if these processes correlate with the SMBH mass (or another variable SMBH mass correlates with, such as spheroid mass/velocity dispersion), and thus the maximum AGN power possible. Some putative processes that could cause nuclear holes in the cold gas distributions (such as shear; see Davis et al. 2018) could naturally follow such a scaling.

(ii) The central structure of the molecular gas in our galaxies has been impacted by AGN feedback, but the black hole is now in a phase of lower activity. If this was the case, a galaxy would be expected to obey the García-Burillo et al. (2021) correlation until its AGN episode dies off, then decrease in X-ray luminosity while presenting its feedback-affected molecular gas structure for some time, before further inflows reset the cycle.

Determining which, if either, of these possibilities is at work in our sample galaxies is interesting, but will require further observations and simulations of molecular gas at the centres of active galaxies of all luminosities.

6 CONCLUSIONS

We have searched for correlations between the cold molecular gas masses on the circumnuclear regions of a sample of 35 nearby galaxies and AGN activity tracers at radio, X-ray, optical and sub-mm wavelengths. We find that the molecular gas masses of our sample
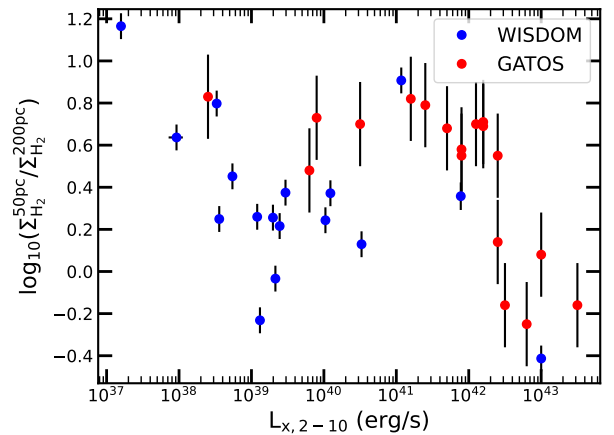
Figure 8. 2-10 keV X-ray luminosity versus nuclear molecular gas concentration. Blue data points are for the sample analysed in this work, red data points are from García-Burillo et al. (2021). The galaxies in our sample do not obey the trend reported in such previous work. This suggests that either the impact of AGN feedback is still detectable in a galaxy when it has gone into a lower activity phase, or the structure of the nuclear molecular gas is not determined by AGN processes.

sources, measured within a range of elliptical apertures with radii from 50 to 100 pc, do not correlate with any of the adopted tracers.

The sample analysed in this study includes galaxies with a range of nuclear activities and global properties, and we are unable to reproduce any of the results found for other AGN-specific sub-samples. This suggests the level of nuclear activity in a given galaxy cannot purely be due the amount of cold gas fuel reservoir around the central SMBH. The fuelling mechanism of active galaxies is not ubiquitous and may vary between AGN types, and timescale variations are likely very important.

We also probed the molecular concentration of the circumnuclear gas discs in our sample galaxies to assess whether they had been impacted by AGN feedback. There is no evidence of a relation between structure on circumnuclear scales and current accretion rate, in contrast to results found for some nearby Seyfert galaxies selected to be in an active phase and despite our objects spanning the same

range in circumnuclear properties. This could indicate that these galaxies were previously in a more active phase that impacted the circumnuclear gas, or that these molecular concentrations arise naturally within circumnuclear gas discs and are not related to AGN processes.

Further observations and theoretical studies are clearly needed to make further progress to determine the link between circumnuclear gas reservoirs and nuclear activity. For instance, dense gas may be better linked to the direct reservoirs for accretion, and expanded sample sizes may help to overcome timescale issues.

DATA AVAILABILITY

The data underlying this article are available in the ALMA archive, at http://almascience.eso.org/aq/. Archival data are available from the NASA/IPAC Extragalactic Database (NED), at https://ned.ipac.caltech.edu/ and Dustpedia, at http://dustpedia.astro.noa.gr/. The data used and the final plots will be shared upon a reasonable request to the first author.

REFERENCES

Alexander D. M., Hickox R. C., 2012, New Astron. Rev., 56, 93
Allen S. W., Dunn R. J. H., Fabian A. C., Taylor G. B., Reynolds C. S., 2006, MNRAS, 372, 21
Antonucci R., 1993, ARA&A, 31, 473
Astropy Collaboration et al., 2013, A&A, 558, A33
Astropy Collaboration et al., 2018, AJ, 156, 123

[5] http://www.astropy.org/
[6] https://matplotlib.org/
[7] https://numpy.org/
[8] https://pandas.pydata.org/

Babyk I. V., McNamara B. R., Tamhane P. D., Nulsen P. E. J., Russell H. R., Edge A. C., 2019, ApJ, 887, 149
Baldwin J. A., Phillips M. M., Terlevich R., 1981, PASP, 93, 5
Balmaverde B., Baldi R. D., Capetti A., 2008, A&A, 486, 119
Becker R. H., White R. L., Helfand D. J., 1994, in Crabtree D. R., Hanisch R. J., Barnes J., eds, Astronomical Society of the Pacific Conference Series Vol. 61, Astronomical Data Analysis Software and Systems III. p. 165
Behar E., Baldi R. D., Laor A., Horesh A., Stevens J., Tzioumis T., 2015, MNRAS, 451, 517
Behar E., Vogel S., Baldi R. D., Smith K. L., Mushotzky R. F., 2018, MNRAS, 478, 399
Best P. N., Heckman T. M., 2012, MNRAS, 421, 1569
Bi S., Feng H., Ho L. C., 2020, ApJ, 900, 124
Blundell K. M., Fabian A. C., Crawford C. S., Erlund M. C., Celotti A., 2006, ApJ, 644, L13
Bolatto A. D., Wolfire M., Leroy A. K., 2013, ARA&A, 51, 207
Bonatto C. J., Pastoriza M. G., 1997, ApJ, 486, 132
Bondi H., 1952, MNRAS, 112, 195
Boroson B., Kim D.-W., Fabbiano G., 2011, ApJ, 729, 12
Bower R. G., Benson A. J., Malbon R., Helly J. C., Frenk C. S., Baugh C. M., Cole S., Lacey C. G., 2006, MNRAS, 370, 645
Buttiglione S., Capetti A., Celotti A., Axon D. J., Chiaberge M., Macchetto F. D., Sparks W. B., 2009, A&A, 495, 1033
Cappellari M., 2013, ApJ, 778, L2
Cappellari M., et al., 2013, MNRAS, 432, 1862
Cavagnolo K. W., McNamara B. R., Nulsen P. E. J., Carilli C. L., Jones C., Bîrzan L., 2010, ApJ, 720, 1066
Ciotti L., Ostriker J. P., 1997, ApJ, 487, L105
Combes F., et al., 2013, A&A, 558, A124
Condon J. J., Cotton W. D., Greisen E. W., Yin Q. F., Perley R. A., Taylor G. B., Broderick J. J., 1998, AJ, 115, 1693
Cook D. O., van Sistine A., Singer L., Kasliwal M. M., Kaplan D., Iptf Collaboration Growth Collaboration 2017, GRB Coordinates Network, 21707, 1
Crawford C. S., Allen S. W., Ebeling H., Edge A. C., Fabian A. C., 1999, MNRAS, 306, 857
Croton D. J., et al., 2006, MNRAS, 365, 11
Davis T. A., Bureau M., Onishi K., Cappellari M., Iguchi S., Sarzi M., 2017, MNRAS, 468, 4675
Davis T. A., et al., 2018, MNRAS, 473, 3818
Davis T. A., et al., 2020, MNRAS, 496, 4061
Davis T. A., et al., 2022, MNRAS, 512, 1522
De Robertis M. M., Osterbrock D. E., 1986, ApJ, 301, 727
Doi A., Inoue Y., 2016, PASJ, 68, 56
Ferrarese L., Merritt D., 2000, ApJ, 539, L9
Fujita Y., Izumi T., Kawakatu N., Nagai H., Hirasawa R., Ikeda Y., 2023, arXiv e-prints, p. arXiv:2303.16927
Galeev A. A., Rosner R., Vaiana G. S., 1979, ApJ, 229, 318
García-Burillo S., et al., 2014, A&A, 567, A125
García-Burillo S., et al., 2021, A&A, 652, A98
Gaspari M., Ruszkowski M., Oh S. P., 2013, MNRAS, 432, 3401
Gaspari M., Brighenti F., Temi P., 2015, A&A, 579, A62
Gaspari M., Temi P., Brighenti F., 2017, MNRAS, 466, 677
Gleisinger R. C., O'Dea C. P., Gallimore J. F., Wykes S., Baum S. A., 2020, ApJ, 905, 42
Grimm H. J., Gilfanov M., Sunyaev R., 2003, MNRAS, 339, 793
Gültekin K., et al., 2009, ApJ, 698, 198
Hardcastle M. J., Evans D. A., Croston J. H., 2007, MNRAS, 376, 1849
Harris C. R., et al., 2020, Nature, 585, 357
Harrison C. M., 2017, Nature Astronomy, 1, 0165
Heckman T. M., Best P. N., 2014, ARA&A, 52, 589
Heckman T. M., Kauffmann G., Brinchmann J., Charlot S., Tremonti C., White S. D. M., 2004, ApJ, 613, 109
Ho L. C., 2008, ARA&A, 46, 475
Ho L. C., Filippenko A. V., Sargent W. L., 1995, ApJS, 98, 477
Hunter J. D., 2007, Computing in Science and Engineering, 9, 90
Izumi T., Kawakatu N., Kohno K., 2016, ApJ, 827, 81

Jarrett T. H., Chester T., Cutri R., Schneider S. E., Huchra J. P., 2003, AJ, 125, 525

Jiménez-Donaire M. J., et al., 2019, ApJ, 880, 127

Kawamuro T., et al., 2022, arXiv e-prints, p. arXiv:2208.03880

Kim D.-W., Fabbiano G., 2004, ApJ, 611, 846

King A., Nixon C., 2015, MNRAS, 453, L46

King A., Pounds K., 2015, ARA&A, 53, 115

King A. R., Pringle J. E., 2007, MNRAS, 377, L25

Komissarov S. S., Gubanov A. G., 1994, A&A, 285, 27

Kormendy J., Ho L. C., 2013, ARA&A, 51, 511

Laing R. A., Bridle A. H., 2013, MNRAS, 432, 1114

Lelli F., Davis T. A., Bureau M., Cappellari M., Liu L., Ruffa I., Smith M. D., Williams T. G., 2022, MNRAS, 516, 4066

Leroy A. K., Walter F., Brinks E., Bigiel F., de Blok W. J. G., Madore B., Thornley M. D., 2008, AJ, 136, 2782

Leroy A. K., et al., 2019, ApJS, 244, 24

Leroy A. K., et al., 2022, ApJ, 927, 149

Liu Y., Jiang D. R., Gu M. F., 2006, ApJ, 637, 669

Magorrian J., et al., 1998, AJ, 115, 2285

Marconi A., Hunt L. K., 2003, ApJ, 589, L21

Marconi A., Risaliti G., Gilli R., Hunt L. K., Maiolino R., Salvati M., 2004, MNRAS, 351, 169

Martini P., Regan M. W., Mulchaey J. S., Pogge R. W., 2003, ApJ, 589, 774

McMullin J. P., Waters B., Schiebel D., Young W., Golap K., 2007, in Shaw R. A., Hill F., Bell D. J., eds, Astronomical Society of the Pacific Conference Series Vol. 376, Astronomical Data Analysis Software and Systems XVI. p. 127

McNamara B. R., Russell H. R., Nulsen P. E. J., Hogan M. T., Fabian A. C., Pulido F., Edge A. C., 2016, ApJ, 830, 79

Molina J., Shangguan J., Wang R., Ho L. C., Bauer F. E., Treister E., 2023, arXiv e-prints, p. arXiv:2304.01017

Morganti R., 2017, Frontiers in Astronomy and Space Sciences, 4, 42

Moustakas J., Kennicutt Robert C. J., Tremonti C. A., Dale D. A., Smith J.-D. T., Calzetti D., 2010, ApJS, 190, 233

Murphy E. J., et al., 2011, ApJ, 737, 67

Narayan R., Yi I., 1995, ApJ, 452, 710

Nayakshin S., Power C., King A. R., 2012, ApJ, 753, 15

Negri A., Posacki S., Pellegrini S., Ciotti L., 2014, MNRAS, 445, 1351

North E. V., et al., 2019, MNRAS, 490, 319

North E. V., et al., 2021, MNRAS, 503, 5179

Ocaña Flaquer B., Leon S., Combes F., Lim J., 2010, A&A, 518, A9

Onishi K., Iguchi S., Davis T. A., Bureau M., Cappellari M., Sarzi M., Blitz L., 2017, MNRAS, 468, 4663

Pizzolato F., Soker N., 2005, ApJ, 632, 821

Pizzolato F., Soker N., 2010, MNRAS, 408, 961

Prandoni I., Laing R. A., de Ruiter H. R., Parma P., 2010, A&A, 523, A38

Reeves J. N., Turner M. J. L., 2000, MNRAS, 316, 234

Rodríguez-Ardila A., Pastoriza M. G., Donzelli C. J., 2000, ApJS, 126, 63

Rosario D. J., et al., 2018, MNRAS, 473, 5658

Ruffa I., et al., 2019a, MNRAS, 484, 4239

Ruffa I., et al., 2019b, MNRAS, 489, 3739

Ruffa I., Prandoni I., Davis T. A., Laing R. A., Paladino R., Casasola V., Parma P., Bureau M., 2022, MNRAS, 510, 4485

Ruffa I., et al., 2023, arXiv e-prints, p. arXiv:2304.06117

Sandstrom K. M., et al., 2013, ApJ, 777, 5

Seth A. C., et al., 2010, ApJ, 714, 713

Shakura N. I., Sunyaev R. A., 1973, A&A, 24, 337

Shlosman I., Frank J., Begelman M. C., 1989, Nature, 338, 45

Smith M. D., et al., 2019, MNRAS, 485, 4359

Smith M. D., et al., 2021a, MNRAS, 500, 1933

Smith M. D., et al., 2021b, MNRAS, 503, 5984

Strong A. W., et al., 1988, A&A, 207, 1

Suzuki T. L., et al., 2016, MNRAS, 462, 181

Tadhunter C. N., Morganti R., di Serego Alighieri S., Fosbury R. A. E., Danziger I. J., 1993, MNRAS, 263, 999

Tremaine S., et al., 2002, ApJ, 574, 740

Urry C. M., Padovani P., 1995, PASP, 107, 803

Veale M., Ma C.-P., Greene J. E., Thomas J., Blakeslee J. P., McConnell N., Walsh J. L., Ito J., 2017, MNRAS, 471, 1428

Wada K., Papadopoulos P. P., Spaans M., 2009, ApJ, 702, 63

Wagner A. Y., Bicknell G. V., Umemura M., 2012, ApJ, 757, 136

Ward S. R., Harrison C. M., Costa T., Mainieri V., 2022, MNRAS, 514, 2936

Wes McKinney 2010, in Stéfan van der Walt Jarrod Millman eds, Proceedings of the 9th Python in Science Conference. pp 56 – 61, doi:10.25080/Majora-92bf1922-00a

Wu Q., Feng J., Fan X., 2018, ApJ, 855, 46

Zhu G., Zaw I., Blanton M. R., Greenhill L. J., 2011, ApJ, 742, 73

pandas development team T., 2022, pandas-dev/pandas: Pandas, doi:10.5281/zenodo.7093122, https://doi.org/10.5281/zenodo.7093122

Table A1. Emission data

Galaxy	$L_{1.4}$ (erg s^{-1})	$\Delta L_{1.4}$ (erg s^{-1})	$E_{1.4}$	$\Delta E_{1.4}$	$L_{X,2-10}$ (erg s^{-1})	$\Delta L_{X,2-10}$ (erg s^{-1})	X-ray Source	L_{mm} (erg s^{-1})	ΔL_{mm} (erg s^{-1})	$\log_{10}\left(\frac{L_{[OIII]}}{\mathrm{erg\,s}^{-1}}\right)$	$\log_{10}\left(\frac{\Delta L_{[OIII]}}{\mathrm{erg\,s}^{-1}}\right)$	K_S (mag)	ΔK_S (mag)
(1)	(2)	(3)	(4)	(5)	(6)	(7)	(8)	(9)	(10)	(11)	(12)	(13)	(14)
FRL49	9.06E+38	9.06E+37	0.90	0.205	1.85E+43	1.85E+42	Chandra	1.92E+39	7.85E+37	42.39	0.04	9.8	0.0100
FRL1146	-	-	-	-	2.58E+43	2.58E+42	XMM	2.44E+39	1.41E+38	40.24	0.07	11	0.00800
MRK567	7.48E+38	7.91E+37	0.29	0.205	-	-	-	5.84E+38	-	-	-	11	0.0450
NGC0383	3.59E+40	3.59E+39	3.3	0.205	3.31E+40	3.31E+39	Chandra	7.86E+40	1.26E+38	39.46	0.04	10	0.00700
NGC0404	5.36E+34	6.99E+33	0.49	0.227	1.58E+37	1.58E+36	Chandra	9.76E+35	3.08E+34	37.69	0.04	10	0.00700
NGC0449	5.55E+38	5.78E+37	0.27	0.205	3.78E+40	3.78E+39	XMM	7.47E+38	3.05E+37	41.50	0.04	12	0.0230
NGC0524	2.80E+36	4.61E+35	-0.27	0.212	3.59E+38	3.59E+37	Chandra	8.81E+38	3.56E+36	37.55	0.04	10	0.0730
NGC0612	1.46E+41	1.47E+40	3.0	0.205	7.76E+41	7.76E+40	Chandra	1.19E+41	2.84E+38	40.03	0.04	9.9	0.0990
NGC0708	3.72E+38	3.72E+37	1.6	0.205	2.45E+39	2.45E+38	Chandra	1.27E+39	1.58E+37	39.10	0.04	12	0.0600
NGC1194	1.18E+37	1.18E+36	1.5	0.871	3.50E+41	3.50E+40	XMM	1.23E+39	2.22E+37	40.03	0.04	11	0.0320
NGC1387	2.64E+36	4.22E+35	-0.18	0.212	2.14E+39	2.14E+38	Chandra	1.17E+38	6.03E+36	-	-	10	0.111
NGC1574	-	-	-	-	-	-	-	3.52E+38	3.50E+36	-	-	10	0.0980
NGC2110	6.34E+38	6.76E+37	-	-	5.13E+42	5.13E+41	Chandra	7.72E+39	1.64E+38	40.41	0.04	10	0.0580
NGC3169	5.43E+37	5.43E+36	0.16	0.205	3.39E+41	3.39E+40	Chandra	3.42E+38	1.07E+37	39.46	0.04	10	0.0920
NGC3351	7.08E+36	7.08E+35	-	-	5.46E+38	5.67E+37	ROSAT	1.81E+37	-	37.28	0.15	9.0	0.0150
NGC3368	1.52E+37	1.52E+36	0.19	0.205	1.98E+39	1.98E+38	ASCA	5.40E+37	-	38.85	0.04	9.5	0.0680
NGC3607	5.67E+36	6.57E+35	0.010	0.206	1.45E+39	1.45E+38	Chandra	3.79E+38	2.31E+37	39.48	0.04	9.5	0.0420
NGC3862	8.13E+40	8.13E+39	-	-	3.92E+41	3.92E+40	Chandra	1.52E+41	3.43E+39	39.20	0.04	11	0.0370
NGC4061	5.70E+39	5.70E+38	3.2	0.205	-	-	-	5.98E+39	4.46E+38	-	-	11	0.0400
NGC4261	3.74E+40	4.12E+39	-	-	1.17E+41	1.17E+40	Chandra	6.28E+41	4.43E+38	39.60	0.04	9.0	0.0150
NGC4429	4.59E+34	2.30E+35	-1.8	2.18	1.31E+39	1.31E+38	Einstein	1.23E+38	9.42E+36	38.69	0.04	10	0.0650
NGC4435	2.72E+36	2.72E+36	-0.010	0.478	2.95E+39	2.95E+38	Chandra	5.69E+37	1.92E+36	39.02	0.04	10	0.0590
NGC4438	2.87E+37	2.87E+36	0.48	0.205	1.20E+38	1.20E+38	Chandra	4.08E+37	9.81E+36	39.69	0.04	8.8	0.0150
NGC4501	9.05E+37	9.05E+36	0.25	0.205	1.23E+40	1.23E+39	Chandra	8.01E+37	4.39E+36	39.31	0.04	9.0	0.0150
NGC4697	1.30E+35	1.08E+35	-1.1	0.413	3.31E+38	3.31E+37	Chandra	1.79E+37	1.65E+36	-	-	9.7	0.0660
NGC4826	9.30E+36	9.03E+35	0.40	0.204	9.23E+37	2.05E+37	Chandra	8.27E+36	1.64E+36	39.03	0.04	8.0	0.0150
NGC5064	1.93E+38	1.93E+37	0.89	0.205	-	-	-	9.19E+37	8.53E+36	-	-	11	0.0730
NGC5765b	5.03E+37	5.03E+37	-0.010	0.205	5.37E+40	5.37E+39	Chandra	1.15E+39	2.17E+38	-	-	10.9	0.0700
NGC5806	1.17E+37	1.17E+36	-0.18	0.205	-	-	-	1.85E+37	-	-	-	11	0.0730
NGC5995	5.91E+38	6.36E+37	-	-	2.45E+43	2.45E+42	Chandra	3.22E+39	1.07E+38	-	-	10	0.0390
NGC6753	3.23E+38	3.53E+37	0.91	0.205	-	-	-	6.73E+37	-	-	-	11	0.0990
NGC6958	2.34E+37	2.81E+36	0.67	0.207	-	-	-	2.92E+39	1.51E+37	-	-	10	0.0600
NGC7052	9.21E+38	9.30E+37	1.8	0.205	1.05E+40	1.05E+39	Chandra	1.35E+40	6.23E+37	39.44	0.04	11	0.0420
NGC7172	7.20E+37	7.66E+36	0.20	0.205	1.00E+43	1.00E+42	Chandra	2.74E+39	1.04E+38	-	-	10	0.0560
PGC043387	-	-	-	-	-	-	-	8.02E+38	-	-	-	10.7	0.0110

Notes: (1) Galaxy name, (2) 1.4GHz luminosity, (3) 1.4GHz luminosity uncertainty, (4) Excess radio fraction, (5) Excess radio fraction uncertainty, (6) 2-10 keV X-ray luminosity, (7) (2-10) keV X-ray luminosity uncertainty, (8) The telescope used for the X-ray observation, (9) Nuclear mm luminosity, (10) Nuclear mm luminosity uncertainty, (11) [OIII] luminosity, (12) [OIII] luminosity uncertainty, (13) K_S-band magnitude, (14) K_S-band magnitude uncertainty.
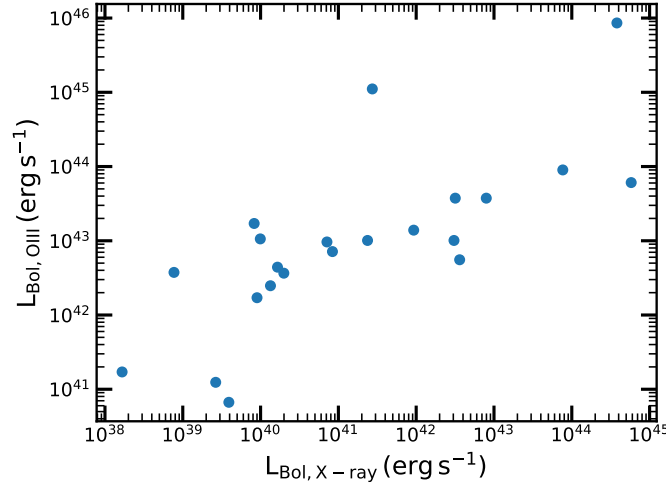
Figure A1. L_{Bol} derived from X-ray versus L_{Bol} derived from [OIII]

APPENDIX A: EMISSION DATA AND DERIVED VALUES

This paper has been typeset from a TeX/LaTeX file prepared by the author.

Table A2. Derived quantities

Galaxy	$\dot{M}_{\text{X-ray,acc}}$ (M$_\odot$ yr^{-1})	$\Delta\dot{M}_{\text{X-ray,acc}}$ (M$_\odot$ yr^{-1})	$\dot{M}_{\text{[OIII],acc}}$ (M$_\odot$ yr^{-1})	$\Delta\dot{M}_{\text{[OIII],acc}}$ (M$_\odot$ yr^{-1})
(1)	(2)	(3)	(4)	(5)
FRL49	5.70E-02	5.70E-03	1.29E+00	1.19E-01
FRL1146	8.70E-02	8.70E-03	9.12E-03	1.47E-03
MRK567	-	-	-	-
NGC0383	3.55E-05	3.55E-06	1.51E-03	1.39E-04
NGC0404	2.50E-08	2.50E-09	2.57E-05	2.37E-06
NGC0449	4.10E-05	4.10E-06	1.66E-01	1.53E-02
NGC0524	3.98E-07	3.98E-08	1.86E-05	1.72E-06
NGC0612	1.19E-03	1.19E-04	5.63E-03	5.18E-04
NGC0708	2.48E-06	2.48E-07	6.61E-04	6.09E-05
NGC1194	4.77E-04	4.77E-05	5.63E-03	5.18E-04
NGC1387	2.17E-06	2.17E-07	-	-
NGC1574	-	-	-	-
NGC2110	1.15E-2	1.15E-3	1.91E-02	1.76E-03
NGC3169	4.60E-04	4.60E-05	1.51E-03	1.39E-04
NGC3351	5.88E-07	6.10E-08	1.00E-05	3.46E-06
NGC3368	2.01E-06	2.01E-07	3.72E-04	3.42E-05
NGC3607	1.49E-06	1.49E-07	1.59E-03	1.46E-04
NGC3862	5.43E-04	5.43E-05	8.32E-04	7.67E-05
NGC4061	-	-	-	-
NGC4261	1.39E-04	1.39E-05	2.09E-03	1.93E-04
NGC4429	1.34E-06	1.34E-07	2.57E-04	2.37E-05
NGC4435	2.98E-06	2.98E-07	5.50E-04	5.06E-05
NGC4438	1.24E-06	1.24E-07	2.57E-03	2.37E-04
NGC4501	1.26E-05	1.26E-06	1.07E-03	9.87E-05
NGC4697	3.68E-07	3.68E-08	-	-
NGC4826	1.16E-07	2.56E-08	5.63E-04	5.18E-05
NGC5064	-	-	-	-
NGC5765b	5.96E-05	5.96E-06	-	-
NGC5806	-	-	-	-
NGC5995	8.14E-02	8.14E-03	-	-
NGC6753	-	-	-	-
NGC6958	-	-	-	-
NGC7052	1.07E-05	1.07E-6	1.45E-03	1.33E-04
NGC7172	2.63E-02	2.63E-03	-	-
PGC043387	-	-	-	-

Notes: (1) Galaxy name. (2) X-ray-traced accretion rate. (3) X-ray-traced accretion rate uncertainty. (4) [OIII]-traced accretion rate. (5) [OIII]-traced accretion rate uncertainty.

Table A3. CO integrated intensity data

Galaxy	I_{CO} (200 pc) (Jy km s^{-1})	ΔI_{CO} (200 pc) (Jy km s^{-1})	I_{CO} (100 pc) (Jy km s^{-1})	ΔI_{CO} (100 pc) (Jy km s^{-1})	I_{CO} (75 pc) (Jy km s^{-1})	ΔI_{CO} (75 pc) (Jy km s^{-1})	I_{CO} (50 pc) (Jy km s^{-1})	ΔI_{CO} (50 pc) (Jy km s^{-1})
(1)	(2)	(3)	(4)	(5)	(6)	(7)	(8)	(9)
FRL49	7.75	0.78	2.39	0.24	-	-	-	-
FRL1146	-	-	-	-	-	-	-	-
MRK567	9.58	0.96	3.98	0.4	-	-	-	-
NGC0383	7.60	0.76	2.74	0.27	1.6	0.16	0.64	0.06
NGC0404	39.62	3.96	39.73	3.97	39.07	3.91	36.14	3.61
NGC0449	-	-	-	-	-	-	-	-
NGC0524	11.64	1.16	3.77	0.38	2.48	0.25	1.29	0.13
NGC0612	2.22	0.22	0.58	0.06	0.44	0.05	0.32	0.04
NGC0708	9.24	0.92	3.18	0.32	2.05	0.21	0.95	0.1
NGC1194	2.58	0.26	1.13	0.11	0.76	0.08	-	-
NGC1387	27.95	2.80	6.8	0.68	3.78	0.38	1.62	0.16
NGC1574	3.98	0.40	3.53	0.35	2.89	0.29	1.6	0.16
NGC2110	4.62	0.46	1.21	0.12	-	-	-	-
NGC3169	125.84	12.58	43.18	4.32	26.99	2.7	-	-
NGC3351	104.99	10.50	55.74	5.57	32.78	3.28	18.57	1.86
NGC3368	170.74	17.07	54.79	5.48	35.54	3.55	19.23	1.92
NGC3607	37.39	3.74	15.56	1.56	10.37	1.04	-	-
NGC3862	-	-	-	-	-	-	-	-
NGC4061	1.21	0.12	0.34	0.03	0.21	0.02	-	-
NGC4261	5.91	0.59	5.49	0.55	4.59	0.46	2.98	0.3
NGC4429	17.38	1.74	3.64	0.36	2	0.2	0.64	0.06
NGC4435	35.67	3.57	15.68	1.57	9.91	0.99	5.28	0.53
NGC4438	134.20	13.42	52.63	5.26	32.86	3.29	15.26	1.53
NGC4501	137.79	13.78	63.66	6.37	40.61	4.06	20.26	2.03
NGC4697	1.90	0.19	1.55	0.16	1.23	0.12	0.74	0.07
NGC4826	276.92	27.69	193.02	19.3	148.73	14.87	74.96	7.5
NGC5064	27.91	2.79	9.7	0.97	5.27	0.53	2.58	0.26
NGC5765b	4.70	0.47	-	-	-	-	-	-
NGC5806	19.20	1.92	7.53	0.75	5.46	0.55	3.09	0.31
NGC5995	-	-	-	-	-	-	-	-
NGC6753	57.58	5.76	19.66	1.97	11.8	1.18	5.65	0.56
NGC6958	12.76	1.28	3.76	0.38	2.3	0.23	1.03	0.11
NGC7052	5.06	0.51	2.2	0.22	1.33	0.13	0.55	0.06
NGC7172	47.03	4.70	6.19	0.62	2.85	0.29	1.14	0.11
PGC043387	-	-	-	-	-	-	-	-

Notes: (1) Galaxy name. (2) 200pc radius aperture integrated CO intensity. (3) 200pc aperture CO intensity uncertainty. (4)-(9) follows the same trend for the 100, 75 and 50 pc radius apertures.

Median values for samples				
	This Work	Garcia-Burillo+21	Izumi+16	Babyk+19
log L_{bol} (erg s^{-1})	43.2	43.0	43.3	-
log M_{BH} (M$_\odot$)	8.04	7.09	7.38	-
log (λ_{edd})	-2.57	-2.20	-2.17	-
log P_{jet} (erg s^{-1})	42.3	-	-	42.3
KS test				
Samples		*p*-values		
This Work-GB+21 (L_{bol})		0.015		
This Work-Izumi+16 (L_{bol})		0.001		
This Work-GB+21 (M_{BH})		0.0003		
This Work-Izumi+16 (M_{BH})		7.27×10^{-5}		
This Work-GB+21 (λ_{edd})		0.03		
This Work-Izumi+16 (λ_{edd})		0.003		
This Work-Babyk+19 (P_{jet})		0.53		

Table A4. Median and KS test *p*-values for the samples used in this work